

Strong and almost strong modes of Floquet spin chains in Krylov subspaces

Daniel J. Yates and Aditi Mitra

*Center for Quantum Phenomena, Department of Physics,
New York University, 726 Broadway, New York, NY, 10003, USA*

(Dated: July 6, 2022)

Integrable Floquet spin chains are known to host strong zero and π modes which are boundary operators that respectively commute and anticommute with the Floquet unitary generating stroboscopic time-evolution, in addition to anticommuting with a discrete symmetry of the Floquet unitary. Thus the existence of strong modes imply a characteristic pairing structure of the full spectrum. Weak interactions modify the strong modes to almost strong modes that almost commute or anticommute with the Floquet unitary. Manifestations of strong and almost strong modes are presented in two different Krylov subspaces. One is a Krylov subspace obtained from a Lanczos iteration that maps the Heisenberg time-evolution generated by the Floquet Hamiltonian onto dynamics of a single particle on a fictitious chain with nearest neighbor hopping. The second is a Krylov subspace obtained from the Arnoldi iteration that maps the Heisenberg time-evolution generated directly by the Floquet unitary onto dynamics of a single particle on a fictitious chain with longer range hopping. While the former Krylov subspace is sensitive to the branch of the logarithm of the Floquet unitary, the latter obtained from the Arnoldi scheme is not. The effective single particle models obtained in the two Krylov subspaces are discussed, and the topological properties of the Krylov chain that ensure stable 0 and π modes at the boundaries are highlighted. The role of interactions is discussed. Expressions for the lifetime of the almost strong modes are derived in terms of the parameters of the Krylov subspace, and are compared with exact diagonalization.

I. INTRODUCTION

The Kitaev chain [1], which after a Jordan-Wigner transformation maps to the transverse field Ising model (TFIM) [2], despite its apparent simplicity, is a toy model for understanding diverse phenomena such as quantum phase transitions [2] and topological systems [3]. It also forms a building block for realizing non-Abelian braiding [4–7]. In recent years, periodic or Floquet driving of this model has helped conceptualize new phenomena such as boundary and bulk discrete time crystals [8–10].

A key feature of the TFIM model, and its anisotropic generalization, is that it hosts robust edge modes known as strong zero modes (SZMs) [1, 11]. An operator Ψ_0 is a SZM if it obeys certain properties. Firstly it should commute with the Hamiltonian H in the thermodynamic limit i.e., $[\Psi_0, H] \approx 0$, secondly it should anticommute with a discrete (say \mathbb{Z}_2) symmetry of the Hamiltonian \mathcal{D} , $\{\Psi_0, \mathcal{D}\} = 0$, and thirdly it should be a local operator with the property $\Psi_0^2 = O(1)$. The presence of a SZM immediately implies that the entire spectrum of H is doubly degenerate, where the degenerate pairs are $\{|n\rangle, \Psi_0|n\rangle\}$, with each member of the pair being eigenstates of \mathcal{D} , but in the opposite symmetry sector. This eigenstate-phase makes the edge modes extremely stable to adding symmetry preserving perturbations, such as exchange interactions between spins. In particular, the edge modes acquire a finite lifetime in the presence of interactions, but with the lifetime being non-perturbative in the strength of the interaction [12–17]. These long-lived quasi-stable modes in the presence of perturbations are referred to as almost strong zero modes (ASZMs) [13].

Under Floquet driving, besides the SZMs, new edge modes arise [18–22], which are called strong π modes

(SPMs) [22], with the possibility of having phases where SZMs and SPMs co-exist [22–26]. In order to define the strong modes in a Floquet system, one needs to adapt the previous definition of the SZM to that of a Floquet unitary over one drive cycle, U . The SZM Ψ_0 and the SPM Ψ_π are now defined as follows. Both these operators anticommute with the discrete symmetry of U , $\{\Psi_0, \mathcal{D}\} = 0$, $\{\Psi_\pi, \mathcal{D}\} = 0$. But while the SZM Ψ_0 commutes with the Floquet unitary in the thermodynamic limit $[\Psi_0, U] \approx 0$, the SPM Ψ_π anticommutes with it $\{\Psi_\pi, U\} \approx 0$ in the same limit. Moreover, as for the static case, both operators are local, with the property $\Psi_{0,\pi}^2 = O(1)$. Thus existence of Ψ_0 implies that the entire spectrum of U is doubly degenerate $\{|n\rangle, \Psi_0|n\rangle\}$, with the two eigenstates of a pair being eigenstates of opposite symmetry. The existence of Ψ_π also implies that the spectrum is paired, but with each pair $|n\rangle, \Psi_\pi|n\rangle$ not only being eigenstates of opposite symmetry, but also being separated by the quasi-energy of π/T , with T being the period of the drive. The existence of SPMs leads to boundary time-crystals.

In the Floquet setting, SZMs and SPMs have been identified in free fermion (integrable) Floquet chains [18, 20, 22]. In addition, the effect of weak interactions were explored using exact diagonalization (ED) where it was found that quasi-stable and long lived edge modes exist despite bulk heating [22]. Drawing inspiration from the static case [13], these quasi-stable modes are called ASZMs and almost strong π modes (ASPMs) [22]. The current paper proposes a route to understanding these quasi-stable modes by mapping their dynamics to a Krylov subspace. A similar study was performed for ASZMs in static chains [16, 17]. Here we generalize this to Floquet chains. Since the Krylov space dynamics is the dynamics of a free particle on a fictitious one-

dimensional (1d) lattice, the Krylov chain, this mapping paves the way for developing analytic methods to extract the lifetimes for general interacting settings.

The paper is organized as follows. The integrable model is introduced in Section II, and its phases outlined. In Section III the Heisenberg time-evolution of the SZM and SPM are mapped to a Krylov subspace via a Lanczos iteration scheme where the generator of the dynamics is the logarithm of the Floquet unitary over one drive cycle, i.e., the Floquet Hamiltonian. The features of the Krylov lattice that ensure stable edge modes are highlighted. In Section IV, the dynamics generated by the Floquet unitary is mapped to a Krylov subspace via the Arnoldi iteration [27]. In section V analytic expressions of the Krylov subspace arising from the Arnoldi method are derived in the free limit. In Section VI, the Arnoldi iteration is used to arrive at a compact expression for the lifetime of the edge modes that holds for finite size systems as well as non-zero interactions. In Section VII, the effect of interactions on the two Krylov subspaces is discussed, and the lifetime of the edge modes obtained from Krylov space methods are compared with ED. We present our conclusions in Section VIII.

II. MODEL

In this section we introduce the integrable model of the Floquet chain. We consider an open chain of length L where the stroboscopic time evolution is generated by the following Floquet unitary [20, 22, 23, 28, 29]

$$U = e^{-i\frac{T}{2}J_x H_{xx}} e^{-i\frac{T}{2}gH_z}, \quad (1)$$

where

$$H_z = \sum_{i=1}^L \sigma_i^z, \quad (2)$$

$$H_{xx} = \sum_{i=1}^{L-1} \sigma_i^x \sigma_{i+1}^x. \quad (3)$$

In what follows we set $J_x = 1$. The Floquet unitary has a discrete symmetry as it commutes with

$$\mathcal{D} = \sigma_1^z \dots \sigma_L^z. \quad (4)$$

When we add interactions in Section VII, \mathcal{D} will continue to be a symmetry of the problem.

Eq. (1) is a binary drive where the first part of the drive involves time-evolution purely by the local magnetic field of strength gT , while the second part of the drive involves time-evolution with respect to the nearest-neighbor Ising interaction of strength T . When $T \ll 1$, the phases of the Kitaev chain are recovered, where as g is tuned from $g < 1$ to $g > 1$, one encounters a quantum phase transition from a topologically non-trivial phase to a topologically trivial phase. We are interested in general T where the phase diagram is much richer. Eventually we

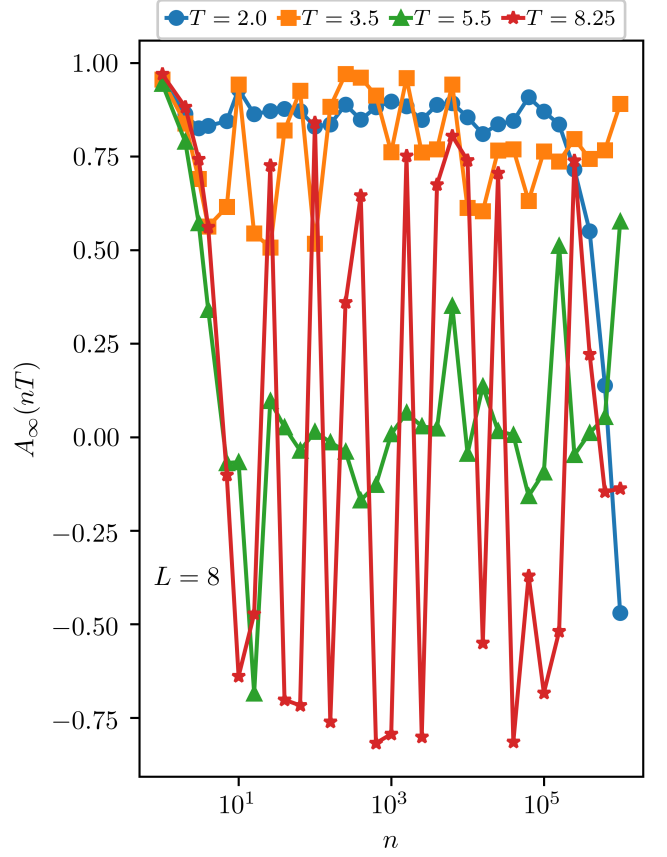


FIG. 1. The autocorrelation function A_∞ at logarithmically separated stroboscopic times for a chain of length $L = 8$ and for the free binary drive. The parameters are $g = 0.3$ and $T = 2.0, 3.5, 5.5, 8.25$ corresponding respectively to SZM phase, SZM-SPM phase, trivial phase, and a SPM phase.

are interested in how these phases manifest in the Krylov subspace, and how interactions modify the Krylov subspace.

It is convenient to map the problem to Majorana fermions as follows

$$a_{2\ell-1} = \prod_{j=1}^{\ell-1} \sigma_j^z \sigma_\ell^x; \quad a_{2\ell} = \prod_{j=1}^{\ell-1} \sigma_j^z \sigma_\ell^y, \quad (5)$$

where $\ell = 1 \dots L$. Denoting the vector

$$\vec{a} = \begin{pmatrix} a_1 \\ a_2 \\ a_3 \\ \vdots \\ a_{2L} \end{pmatrix}, \quad (6)$$

the stroboscopic time-evolution of \vec{a} is as follows

$$U^\dagger \vec{a} U = K \vec{a}, \quad (7)$$

where on defining

$$c_1 = \cos(Tg), \quad (8a)$$

$$c_2 = \cos(T), \quad (8b)$$

$$s_1 = \sin(Tg), \quad (8c)$$

$$s_2 = \sin(T), \quad (8d)$$

we find that K takes the following form [22] for $L = 3$

$$K = \begin{pmatrix} c_1 & -s_1 & 0 & 0 & 0 & 0 \\ s_1 c_2 & c_1 c_2 & -c_1 s_2 & s_1 s_2 & 0 & 0 \\ s_1 s_2 & c_1 s_2 & c_1 c_2 & -s_1 c_2 & 0 & 0 \\ 0 & 0 & s_1 c_2 & c_1 c_2 & -c_1 s_2 & s_1 s_2 \\ 0 & 0 & s_1 s_2 & c_1 c_2 & c_1 c_2 & -s_1 c_2 \\ 0 & 0 & 0 & 0 & s_1 & c_1 \end{pmatrix}. \quad (9)$$

K is an orthogonal matrix which, depending on the parameters can admit eigenvalues at ± 1 . While K has been shown explicitly for $L = 3$, the form for general L can be easily guessed as the bulk consisting of the second and third rows are repeated. For the example of $L = 3$ given above, we see that the bulk structure is repeated twice.

A key quantity that we will analyze is the autocorrelation function of $\sigma_1^x = a_1$, evaluated at stroboscopic times

$$A_\infty(nT) = \frac{1}{2L} \text{Tr} \left[\sigma_1^x(nT) \sigma_1^x(0) \right], \quad (10a)$$

$$\sigma^x(nT) = [U^\dagger]^n \sigma_1^x U^n. \quad (10b)$$

When strong modes exist, this quantity has a non-zero overlap with them, and therefore its stroboscopic time-evolution is a diagnostic for whether strong modes exist or not. Moreover, from Eq. (7) it is clear that the above autocorrelation function is completely determined by the action of K on an initial vector that is localized on the first site. Thus ± 1 eigenvalues of K imply SZMs and SPMs respectively.

We discuss some exactly solvable limits. Below n is an integer.

- $Tg = (2n+1)\pi$, T arbitrary: We have $e^{-iTgH_z/2} \propto \mathcal{D}$, thus $U^\dagger \sigma_1^x U = \mathcal{D} \sigma_1^x \mathcal{D} = -\sigma_1^x$, and a SPM exists. There is however no SZM.
- $Tg = (2n)\pi$, T arbitrary: Now $e^{-iTgH_z/2} \propto 1$, thus $U^\dagger \sigma_1^x U = \sigma_1^x$. We now have a SZM while there is no SPM.
- $T = (2n+1)\pi$, Tg arbitrary: Now we have $e^{-iTgH_z/2} \propto \sigma_1^x \sigma_L^x$. With $e^{-iTgH_z/2} = \prod_{i=1}^L [\cos(Tg/2) - i\sigma_i^z \sin(Tg/2)]$. It is straightforward to check that

$$\begin{aligned} U^\dagger \sigma_1^x U &= \cos(Tg) \sigma_1^x - \sin(Tg) \sigma_1^y, \\ U^\dagger \sigma_1^y U &= -\sin(Tg) \sigma_1^x - \cos(Tg) \sigma_1^y. \end{aligned} \quad (11)$$

The above linear combinations of σ_1^x and σ_1^y yield a SZM and a SPM.

- $T = 2n\pi$, Tg arbitrary: We have $e^{-iTgH_z/2} \propto 1$. Then,

$$\begin{aligned} U^\dagger \sigma_1^x U &= \cos(Tg) \sigma_1^x - \sin(Tg) \sigma_1^y, \\ U^\dagger \sigma_1^y U &= \sin(Tg) \sigma_1^x + \cos(Tg) \sigma_1^y. \end{aligned} \quad (12)$$

The above linear combinations do not yield any strong modes unless $Tg = m\pi$ where m is any integer. Here two cases arise depending on whether m is even or odd. If $Tg = 2m\pi$ then σ_1^x is trivially a SZM because $U \propto 1$. If $Tg = (2m+1)\pi$, then σ_1^x is a SPM because $U \propto \mathcal{D}$.

The above examples show that whenever a SPM exists, the Floquet unitary has a characteristic non-local structure by either being of the form $U \propto \mathcal{D}$ (SPM phase) or being of the form $U \propto \sigma_1^x \sigma_L^x$ (SZM-SPM phase) [23–26]. We will show later that this non-local structure will have implications on the Krylov subspace.

The above phases are stable to perturbing around it. Fig. 1 shows A_∞ for some special cases for stroboscopic and logarithmically separated times. The parameters chosen are $g = 0.3$, and $T = 2.0, 3.5, 5.5, 8.25$. We will work with these parameters for the rest of the paper when presenting the numerical results. Among the chosen parameters, all of them except $T = 5.5$ host strong modes. Thus for all parameters except $T = 5.5$, A_∞ is long-lived with its lifetime only set by the system size L . Among these different cases, $T = 2.0$ is a phase that has a SZM, $T = 3.5$ is a phase that simultaneously hosts a SZM and a SPM, while $T = 8.25$ hosts a SPM. For a SPM, the stroboscopic time-evolution flips between $O(1)$ positive and negative values, consistent with period-doubled dynamics.

When both SZM and SPM exist, σ_1^x has an overlap with both of them. Thus we can write, $\Psi_0 = a\sigma_1^x + \dots$ and $\Psi_\pi = b\sigma_1^x(-1)^n + \dots$ where $a, b = O(1)$ and positive $a, b > 0$. After the initial transients, we can write the form of $\sigma_1^x(t)$ as $\sigma_1^x(t) \approx c_0 \Psi_0 + c_\pi \Psi_\pi + \dots$, where $c_0, c_\pi \leq 1/2$ for normalization. Thus the autocorrelation function becomes $A_\infty(nT) \approx c_0 a + c_\pi b(-1)^n$. This shows that the signal will oscillate between $c_0 a + c_\pi b$ and $c_0 a - c_\pi b$. There are several indications that $c_0 > c_\pi$. Firstly, note from Fig. 1 that when only a SZM is present, $c_0 \approx 1$, while when only a SPM is present $c_\pi \approx 0.75$. This is further corroborated at the exactly solvable limit for the SZM-SPM phase discussed in Eq. (11). Here one finds that at odd stroboscopic times $A_\infty(n=1) = \cos(gT)$, while at even stroboscopic times $A_\infty(n=2) = 1$. Since $c_0 > c_\pi$, the signal oscillates between two positive numbers, as shown in Fig. 1.

Let us define the Floquet Hamiltonian H_F as

$$H_F = \frac{i}{T} \ln(U). \quad (13)$$

Note that for the binary drive in Eq. (1), since the problem is free, the matrix K in Eq. (7) and U are simultaneously diagonalized. Thus $i \ln K$ directly gives us the

Floquet Hamiltonian H_F in the Majorana basis. We now discuss the structure of K , and in particular $i \ln K$ for three different phases, one that supports a SZM, one that supports a SPM, and one that simultaneously supports a SZM and a SPM.

A. $i \ln K$ for $Tg \ll 1$, $T \ll 1$: SZM phase

In this section we derive an analytic expression for $i \ln K$ for $Tg \ll 1$ and in the high frequency limit of $T \ll 1$. Note that when $Tg = 0$ the coefficients in Eq. (8) become, $s_1 = 0, c_1 = 1$ while s_2, c_2 are arbitrary. This gives

$$K_0 = \begin{pmatrix} 1 & 0 & 0 & 0 & 0 & 0 \\ 0 & c_2 & -s_2 & 0 & 0 & 0 \\ 0 & s_2 & c_2 & 0 & 0 & 0 \\ 0 & 0 & 0 & c_2 & -s_2 & 0 \\ 0 & 0 & 0 & s_2 & c_2 & 0 \\ 0 & 0 & 0 & 0 & 0 & 1 \end{pmatrix}. \quad (14)$$

Due to the block-diagonal form of K_0 , it is straightforward to diagonalize it, take its logarithm, and rotate back to the original basis. This gives

$$\ln K_0 = -iT \begin{pmatrix} 0 & 0 & 0 & 0 & 0 & 0 \\ 0 & 0 & -i & 0 & 0 & 0 \\ 0 & i & 0 & 0 & 0 & 0 \\ 0 & 0 & 0 & 0 & -i & 0 \\ 0 & 0 & 0 & i & 0 & 0 \\ 0 & 0 & 0 & 0 & 0 & 0 \end{pmatrix}. \quad (15)$$

Now writing $K = K_0 + V_p$ we find

$$V_p = \begin{pmatrix} 0 & -s_1 & 0 & 0 & 0 & 0 \\ s_1 c_2 & 0 & 0 & s_1 s_2 & 0 & 0 \\ s_1 s_2 & 0 & 0 & -s_1 c_2 & 0 & 0 \\ 0 & 0 & s_1 c_2 & 0 & 0 & s_1 s_2 \\ 0 & 0 & s_1 s_2 & 0 & 0 & -s_1 c_2 \\ 0 & 0 & 0 & 0 & s_1 & 0 \end{pmatrix} + O(s_1^2). \quad (16)$$

If we now also impose that $T \ll 1$ or equivalently $s_2 \ll 1$, then K_0 and V_p are two matrices whose commutator is $O(s_1 s_2) \ll 1$. Recall that if A and B are two commuting matrices $[A, B] = 0$, then,

$$\ln(A + B) \approx \ln[A] + [A]^{-1} B + \dots \quad (17)$$

Neglecting terms of $O(s_1 s_2), O(s_1^2), O(s_2^2)$ and higher, we have two commuting matrices $A = K_0, B = V_p$. We can then use Eq. (17) to obtain the following expression to first order in s_1 and T

$$i \ln K \approx \begin{pmatrix} 0 & -is_1 & 0 & 0 & 0 & 0 \\ is_1 & 0 & -iT & 0 & 0 & 0 \\ 0 & iT & 0 & -is_1 & 0 & 0 \\ 0 & 0 & is_1 & 0 & -iT & 0 \\ 0 & 0 & 0 & iT & 0 & -is_1 \\ 0 & 0 & 0 & 0 & is_1 & 0 \end{pmatrix}. \quad (18)$$

Note that $i \ln K$ or equivalently H_F is identical to a Su-Schrieffer-Heeger (SSH) model [30, 31] with topologically non-trivial dimerization for $|s_1| < T$. Thus the model is guaranteed to host a SZM.

B. $i \ln K$ when $Tg \approx \pi$, $T \ll 1$: SPM phase

We now turn to the phase that hosts a SPM. Denoting $K = K_0$ when $Tg = \pi$, and noting that at this point $s_1 = 0, c_1 = -1$, we have

$$K_0 = \begin{pmatrix} -1 & 0 & 0 & 0 & 0 & 0 \\ 0 & -c_2 & s_2 & 0 & 0 & 0 \\ 0 & -s_2 & -c_2 & 0 & 0 & 0 \\ 0 & 0 & 0 & -c_2 & s_2 & 0 \\ 0 & 0 & 0 & -s_2 & -c_2 & 0 \\ 0 & 0 & 0 & 0 & 0 & -1 \end{pmatrix} = \begin{pmatrix} -1 & 0 & 0 & 0 & 0 & 0 \\ 0 & -e^{-iT\sigma_y} & 0 & 0 & 0 & 0 \\ 0 & 0 & 0 & 0 & 0 & 0 \\ 0 & 0 & 0 & -e^{-iT\sigma_y} & 0 & 0 \\ 0 & 0 & 0 & 0 & 0 & 0 \\ 0 & 0 & 0 & 0 & 0 & -1 \end{pmatrix} \quad (19)$$

Taking the logarithm of the above quantity, one obtains

$$\ln K_0 = -iT \begin{pmatrix} 0 & 0 & 0 & 0 & 0 & 0 \\ 0 & 0 & -i & 0 & 0 & 0 \\ 0 & i & 0 & 0 & 0 & 0 \\ 0 & 0 & 0 & 0 & -i & 0 \\ 0 & 0 & 0 & i & 0 & 0 \\ 0 & 0 & 0 & 0 & 0 & 0 \end{pmatrix} \pm i\pi. \quad (20)$$

The above equation is identical to $\ln K_0$ obtained for the SZM phase (see Eq. (15)), with the difference being that there is an overall shift of the energy by $\pm\pi$ for the SPM. This shift is associated with the fact that K_0 for the SZM and K_0 for the SPM differ by an overall phase of -1 at odd stroboscopic times.

We now write $K = K_0 + V_p$ where

$$V_p = \begin{pmatrix} 0 & -s_1 & 0 & 0 & 0 & 0 \\ s_1 c_2 & 0 & 0 & s_1 s_2 & 0 & 0 \\ s_1 s_2 & 0 & 0 & -s_1 c_2 & 0 & 0 \\ 0 & 0 & s_1 c_2 & 0 & 0 & s_1 s_2 \\ 0 & 0 & s_1 s_2 & 0 & 0 & -s_1 c_2 \\ 0 & 0 & 0 & 0 & s_1 & 0 \end{pmatrix} + O(s_1^2). \quad (21)$$

If we now also impose that $T \ll 1$ so that $s_2 \ll 1$, then K_0 and V_p commute if terms of $O(s_1 s_2), O(s_1^2), O(s_2^2)$ and higher are neglected. Denoting $A = K_0, B = V_p$, we can use Eq. (17) to obtain the following expression to first

order in s_1 and T

$$i \ln K \approx \begin{pmatrix} 0 & is_1 & 0 & 0 & 0 & 0 \\ -is_1 & 0 & -iT & 0 & 0 & 0 \\ 0 & iT & 0 & is_1 & 0 & 0 \\ 0 & 0 & -is_1 & 0 & -iT & 0 \\ 0 & 0 & 0 & iT & 0 & is_1 \\ 0 & 0 & 0 & 0 & -is_1 & 0 \end{pmatrix} \pm \pi. \quad (22)$$

Comparing Eq. (18) and Eq. (22), we find that $i \ln K$ or equivalently the Floquet Hamiltonian in the Majorana basis, has an overall $\pm\pi$ additive term for the SPM phase as compared to the SZM phase. There is also a change in the sign of s_1 between the two equations. However for $|s_1| < T$, the dimerization in Eq. (22) corresponds to that of the topologically non-trivial SSH model. This ensures an edge mode, which due to the additive term will now

be pinned at $\pm\pi$ energy rather than zero energy.

C. K when $T \approx \pi$: SZM-SPM phase

When $T = \pi$, the quantities s_2, c_2 are $s_2 = 0, c_2 = -1$, while s_1, c_1 are arbitrary. Denoting $K = K_0$ at the special point $T = \pi$, we have

$$K_0 = \begin{pmatrix} c_1 & -s_1 & 0 & 0 & 0 & 0 \\ -s_1 & -c_1 & 0 & 0 & 0 & 0 \\ 0 & 0 & -c_1 & s_1 & 0 & 0 \\ 0 & 0 & -s_1 & -c_1 & 0 & 0 \\ 0 & 0 & 0 & 0 & -c_1 & s_1 \\ 0 & 0 & 0 & 0 & s_1 & c_1 \end{pmatrix}. \quad (23)$$

Thus we see that the edge-structure is more complex as what qualifies for the left edge is now the first two sites while the right edge corresponds to the last two sites.

Taking the logarithm of K_0 is tedious but straightforward giving

$$i \ln K_0 = \pm\pi \times \begin{pmatrix} \frac{1-c_1}{2} & \frac{s_1}{2} & 0 & 0 & 0 & 0 \\ \frac{s_1}{2} & \frac{1+c_1}{2} & 0 & 0 & 0 & 0 \\ 0 & 0 & 0 & 0 & 0 & 0 \\ 0 & 0 & 0 & 0 & 0 & 0 \\ 0 & 0 & 0 & 0 & \frac{1+c_1}{2} & \frac{-s_1}{2} \\ 0 & 0 & 0 & 0 & \frac{-s_1}{2} & \frac{1-c_1}{2} \end{pmatrix} + \begin{pmatrix} 0 & 0 & 0 & 0 & 0 & 0 \\ 0 & 0 & 0 & 0 & 0 & 0 \\ 0 & 0 & 0 & -iT \pm i\pi & 0 & 0 \\ 0 & 0 & iT \pm i\pi & 0 & 0 & 0 \\ 0 & 0 & 0 & 0 & 0 & 0 \\ 0 & 0 & 0 & 0 & 0 & 0 \end{pmatrix} \quad (24)$$

At this special point we note that each edge has a zero mode and a π mode that are completely decoupled from the bulk, the latter corresponding to a topologically non-trivial SSH chain. Deviating from this special point will couple the edge mode to the bulk, and also generate longer-range hopping in the Floquet Hamiltonian. However as long as the bulk gap does not close, the edge modes will be robust.

In the remaining paper we discuss the manifestation of the edge modes in Krylov subspaces, and we also include the effect of interactions in these subspaces.

III. KRYLOV CHAIN FROM THE LANCZOS ITERATION

The time evolution of an operator in a generic integrable or non-integrable system can be mapped to single particle dynamics on a semi-infinite chain employing a recursive Lanczos scheme [32]. This method has made a reappearance recently as a way to identify chaotic dynamics [33–36]. In this section we outline this method. The exponential complexity of solving the dynamics enters into the calculation of the hopping parameters on this chain which we denote by b_n .

Note the definition of the Floquet Hamiltonian H_F in Eq. (13). The stroboscopic time-evolution after m periods can be written in terms of H_F as follows

$$[U^\dagger]^m O U^m = e^{iH_F m T} O e^{-iH_F m T} = \sum_{n=0}^{\infty} \frac{(imT)^n}{n!} \mathcal{L}^n O, \quad (25)$$

where we define

$$\mathcal{L}O = [H_F, O]. \quad (26)$$

To employ the Lanczos algorithm, we recast the operator dynamics into vector dynamics by defining $|O\rangle = O$. Since we are concerned with infinite temperature quantities, we have an unambiguous choice for an inner product on the level of the operators,

$$\langle A|B\rangle = \frac{1}{2L} \text{Tr} [A^\dagger B]. \quad (27)$$

The Lanczos algorithm iteratively finds the operator basis that tri-diagonalizes \mathcal{L} . We begin with the seed “state”, $|O_1\rangle$, and let $\mathcal{L}|O_1\rangle = b_1|O_2\rangle$, where $b_1 = \sqrt{|\mathcal{L}|O_1\rangle|^2}$. The recursive definition for the basis operators $|O_{n \geq 2}\rangle$ is,

$$\mathcal{L}|O_n\rangle = b_n|O_{n+1}\rangle + b_{n-1}|O_{n-1}\rangle, \quad (28)$$

where we define $b_n = \sqrt{|\mathcal{L}|O_n|^2}$. It is straightforward algebra to check that the above procedure will iteratively find basis operators that yield a \mathcal{L} which is tri-diagonal, and of the following form,

$$\mathcal{L} = \begin{pmatrix} & b_1 & & \\ b_1 & & b_2 & \\ & b_2 & & \ddots \\ & & \ddots & \end{pmatrix}. \quad (29)$$

This basis spanned by $|O_n\rangle$ lies within the Krylov subspace of \mathcal{L} and $|O_1\rangle$. We refer to this tri-diagonal matrix as the Krylov Hamiltonian H_K ,

$$H_K = \sum_n b_n (c_n^\dagger c_{n+1} + c_{n+1}^\dagger c_n), \quad (30)$$

and the $1d$ lattice it represents, the Krylov chain.

An important aspect of this technique, often overlooked when discussing chaos, is that the values of b_n are highly dependent on the choice of seed operator. Further, outside of special cases, namely a Hamiltonian that is free, the exact solution to the operation $\mathcal{L}|O_n\rangle$ will require ED, or similar methods with equivalent costs. This method does not escape the rapidly growing exponential wall of complexity. In cases where the calculation of all b_n are possible, the above algorithm will return a value of $b_{\text{end}} = 0$.

For free systems, the operation $\mathcal{L}|O_n\rangle$ can be efficiently solved when in the Majorana basis. If the starting operator is a single Majorana then the dimension of the Krylov subspace of that operator will scale as $2L$, as free system dynamics can only mix the individual Majoranas among themselves. Outside of free problems, the size of the full set of $|O_n\rangle$ will be large. For example, a system size of L will have $\sim 2^{2L}$ possible basis operators. For all intents and purposes we treat \mathcal{L} as a semi-infinite chain. If the number of solved b_n is insufficient for the quantity of interest, an approach that works well is to supplement the known set with approximate b_n that are calculated based off of trends established among the known hoppings [16, 17].

Starting with the seed state $|O_1\rangle = |\sigma_1^x\rangle$, we can recast A_∞ into the following form

$$A_\infty(nT) = (e^{i\mathcal{L}nT})_{1,1}. \quad (31)$$

Now, following the above discussion, the dynamics of A_∞ has been transformed into that of a semi-infinite single-particle problem. The details of the semi-infinite chain will be discussed in subsequent sections. Ref. 16 showed that the slow dynamics of A_∞ for static spin chains was a result of topological modes residing at the left boundary (origin) of the Krylov chain. We discuss the analogous situation for the Floquet problem.

Since for the binary drive, the problem is free, the matrix K in Eq. (7) and U are simultaneously diagonalized. Thus we construct the Krylov Hamiltonian by taking the

Floquet Hamiltonian to be $TH_F = i\ln(K)$ and performing the iterative steps outlined above. The parameters b_n of the Krylov Hamiltonian, and the corresponding spectra are shown in Fig. 2. The eigenfunctions with eigenvalues corresponding to 0 and $\pm\pi$ are shown in Fig. 3.

Fig. 2 clearly shows that the Krylov chain has a dimerized structure like that of a SSH chain. The case of the SZM phase at $T = 2.0$ and the trivial phase at $T = 5.5$ are the easiest to understand as these correspond to SSH chains of opposite sign of the dimerization, one sign being topologically trivial ($T = 5.5$) and the other being topologically non-trivial ($T = 2.0$). For the case of the SPM at $T = 8.25$ one finds that the very first site is pinned at a large value of $O(\pi)$, while the rest of the chain, from $n \geq 4$ onwards has a topologically non-trivial dimerization implying an edge mode. The local strong pinning at the first site results in an edge mode that is pinned at $\pm\pi$. Thus π modes of the Floquet chain appear as regular zero modes of the topologically non-trivial Krylov chain with an overall shift in energy by π . For the more complicated SZM-SPM phase at $T = 3.5$, the first two sites at the edges act as a two-level system that can host a pair of edge modes. These modes act as the boundary of an SSH chain with non-trivial sign of the dimerization.

Fig. 3 plots the mod-square of edge modes at 0 and $\pm\pi$ energies ($|\psi_{0,\pi}(n)|^2$) for all the phases. Note that these modes appear in pairs in that, when a zero edge mode exists, there are two of them (orange and blue lines in the upper panels of the plot). While when a π mode exists, there are a pair of them located at π and $-\pi$ (orange and blue lines in the lower panels of the plot). The periodicity of the spectrum under Floquet driving implies that the π modes are doubly degenerate in the same way as the 0 modes are because $-\pi = \pi + 2\pi n$, where n is any integer.

Fig. 3 shows that the degenerate pairs of edge modes are not symmetrically localized on the two ends of the Krylov chain as the chain is constructed for the operator σ_1^x , and is therefore heavily weighted on the left edge. If the seed operator would have been a symmetric linear combination of operators on the first and the last site of the physical chain, then the edge modes of the Krylov chain would also have been symmetrically located at the two ends of the chain. However it is interesting to note that the π edge mode pairs are a lot more asymmetric than the 0 edge mode pairs, where for the latter one does see two peaks, one each on the left and right edges of the Krylov chain. In contrast the π edge mode pairs are strongly peaked at the left edge. This is because of the highly non-local structure of the Floquet unitary when a π mode exists. Recall that in the previous section we showed that when a SPM exists, the Floquet unitary is proportional to the non-local operators \mathcal{D} (SPM phase) or $\sigma_1^x \sigma_L^x$ (SZM-SPM phase), and therefore has weight on the entire chain. Thus the very first Lanczos step, even when it starts out with an operator localized at the left edge, does end up “seeing” the right end of the chain, resulting in the manifestation of the right edge mode on the left edge of the Krylov chain.

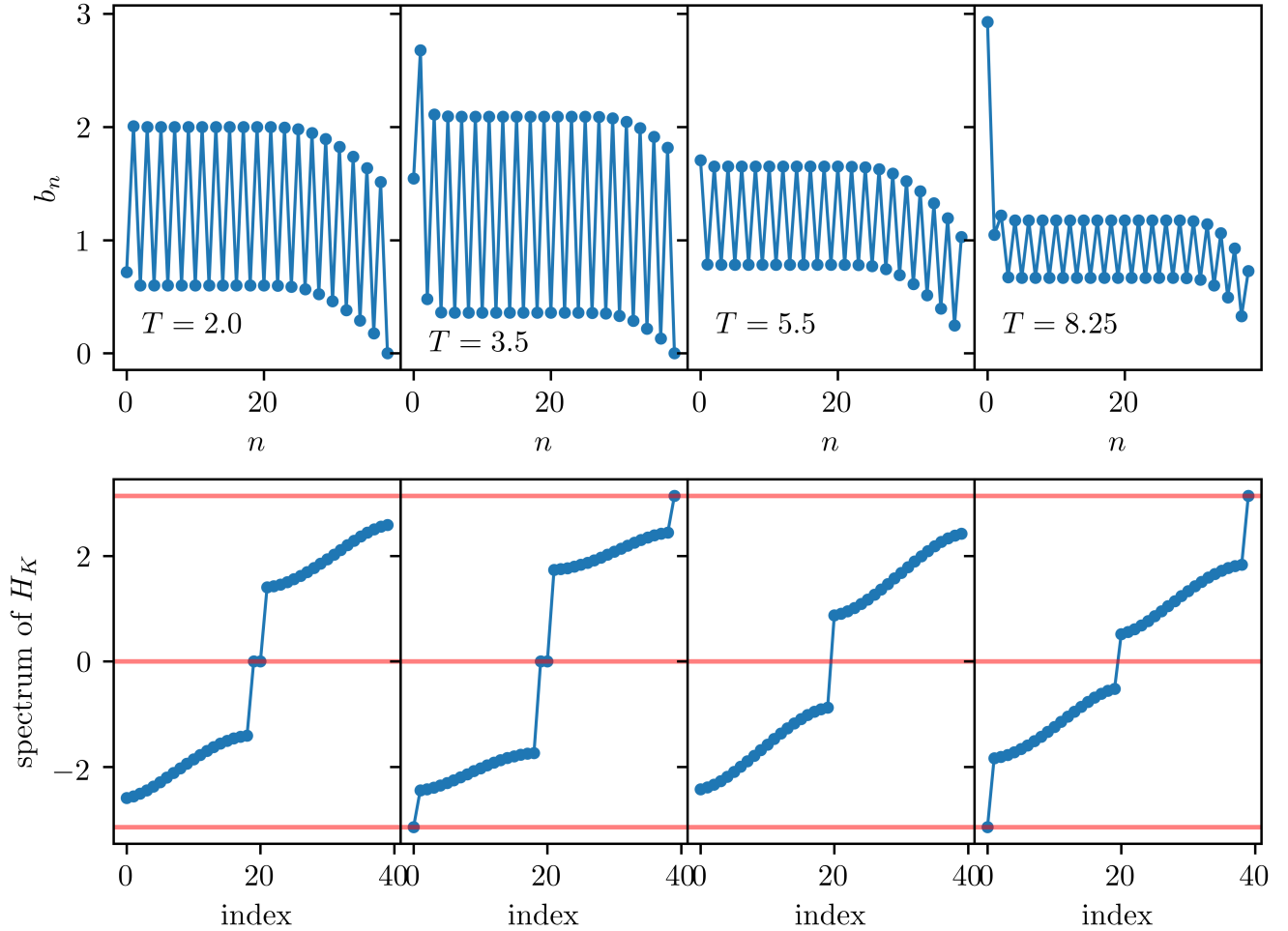


FIG. 2. Upper panel: The b_n s for the binary drive with $g = 0.3$ and system size $L = 20$. Lower panel: The corresponding spectra. For both upper and lower panels, from left to right $T = 2.0, 3.5, 5.5, 8.25$. These parameters correspond to SZM, SZM-SPM, trivial, and SPM phases respectively. Horizontal red lines in lower columns correspond to energies 0 and $\pm\pi$ in units of T^{-1} .

A. Majorana basis vs spin basis

Fig. 4 constructs the Krylov Hamiltonian for the binary drive in a few different ways. The first method is to work in the Majorana basis and to use the Lanczos method where the generator of stroboscopic dynamics is $i\ln K$, where K is given in Eq. (9). For this case, the Lanczos method is a simple basis rotation and the spectrum of the Krylov Hamiltonian H_K , will be exactly the same as that of $i\ln K$. That is, we begin with a single-particle propagator $i\ln K$, and we end with a single-particle propagator \mathcal{L} . The orange data labeled as “free” in Fig. 4 corresponds to this case where all the computations are done in the Majorana basis.

The second way to perform the Lanczos iteration is to work in the many-body or spin basis, even though the problem is free. In this case, we are concerned with the branch of the many-body Floquet Hamiltonian $i\ln U$, and not of the single-particle Hamiltonian $i\ln K$. In

Fig. 4, the blue data set labeled as “spin₁” corresponds to Lanczos performed with $H_F = i\ln U$ without any special treatment for the single-particle status of the problem. The seed state is σ_1^x and after $2L$ iterations of the Lanczos algorithm, it terminates after exhausting all of the Krylov space of σ_1^x . We see the resulting spectrum of H_K in the middle panel extends beyond the Floquet Brillouin zone (FBZ) $[-\pi, \pi]$ as indicated by the horizontal red lines which pass through energies $\pm\pi$. The b_n are shown in the top row and share little in common with the b_n from the Majorana or free basis, which are shown by the orange crosses.

We can now wrap the blue spectrum of H_K such that it fits within the FBZ. This is now given by the green data set labeled “spin₂” in the middle panel. After this wrapping, the Krylov Hamiltonian is no longer tri-diagonal [37], and one needs to perform a second Lanczos iteration to return to a tri-diagonal Krylov subspace. The resulting b_n of this new H_K are shown in the top panel

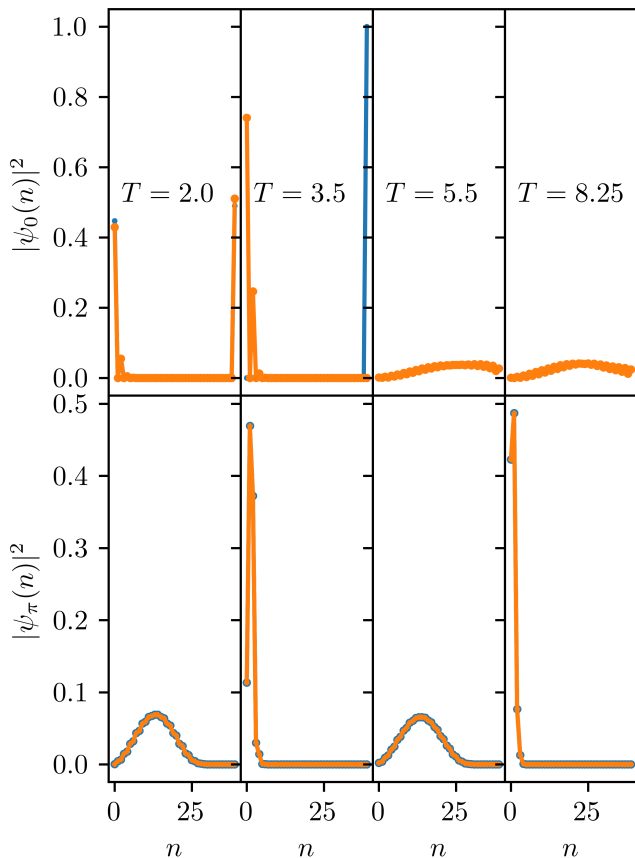


FIG. 3. The mod-square of the eigenfunctions of the Krylov chain for the same parameters as Fig. 2. Upper (lower) panels correspond to edge modes at zero ($\pm\pi$) energy. The orange and blue data sets in each panel reflect the fact that these modes appear in pairs. In particular, there are two zero modes and two π modes, the latter occurring at $\pm\pi$ energy. The plots show that $T = 5.5$ hosts no edge modes, consistent with a trivial phase. On the other hand $T = 2.0$ hosts a pair of edge modes at zero and no edge modes at π . $T = 8.25$ hosts a pair of edge modes at $\pm\pi$ but no edge modes at 0 energy. $T = 3.5$ hosts edge modes at both 0 and $\pm\pi$ energies.

in green, and are labeled as “spin₂”. We note that this wrapping of the spectrum requires us to fully diagonalize the problem, which will typically not be possible for us when dealing with large system sizes. We see that the green b_n of the top row match the b_n obtained from the single-particle Majorana basis upto $b_{n=2L-1}$. At $n = 2L$, $b_{2L} = 0$ so that all the b_n appearing after that represent a second chain decoupled from the part that lies between $n = 1 \dots 2L - 1$. The significance of these decoupled chains on the spectrum is shown in the middle panel (green data). Here we see that the spectrum is repeated twice for our example. This repetition does not influence the physics, as can be seen in the lower panel which plots A_∞ . This is because once $b_m = 0$, the remaining $b_{n>m}$ do not affect the dynamics.

The bottom panel in Fig. 4 plots A_∞ from ED (labeled

“ED”) along with that obtained from the Krylov Hamiltonian Eq. (31). For the latter, the dynamics involves three different H_K , labeled “free”, “spin₁” and “spin₂” with the corresponding b_n shown in the top panels. The plot shows that all of them give the same dynamics, despite the spectra and the b_n being different.

Thus while the b_n and the spectra (top and center rows of Fig. 4) are sensitive to whether the Lanczos is performed on the level of the many-body or spin basis versus the single-particle or Majorana basis, the dynamics is not sensitive to it.

As touched upon in the previous paragraph, to align the free Majorana picture and the free spin picture, we needed to wrap the spectrum of H_K , requiring the full diagonalization of H_K . This is only possible in the free case where we can easily find the full Krylov subspace of the seed operator. Moreover, the reason for the very different b_n in the spin and in the Majorana bases, arises due to the ambiguity associated with the branch of $H_F = i \ln(U)/T$. To avoid this ambiguity, it is better to set up the problem in an alternate Krylov subspace that involves working directly with the Floquet unitary U , rather than with the Floquet Hamiltonian H_F . We discuss this alternate approach in the next section.

IV. KRYLOV CHAIN FROM THE ARNOLDI ITERATION

We now discuss a different Krylov subspace, one that arises from the action of U on the seed operator and is known as the Arnoldi iteration [27]. This differs from the previous section where the generator of the dynamics was a Hermitian operator, the Floquet Hamiltonian $i \ln U$. We instead now work with a unitary operator, and below we outline the steps for obtaining the corresponding Krylov subspace.

Instead of \mathcal{L} , we now have the quantity W which is defined as follows

$$W|O\rangle = U^\dagger \hat{O} U \quad (32)$$

$$W^n|O\rangle = U(n)^\dagger \hat{O} U(n). \quad (33)$$

W is unitary because

$$W^\dagger W|O\rangle = U(U^\dagger \hat{O} U)U^\dagger \quad (34)$$

$$= \hat{O} = WW^\dagger|O\rangle. \quad (35)$$

We now outline the Arnoldi method. This reduces to the Lanczos scheme outlined in the previous section when W is Hermitian. In particular we will see that the unitarity of W will no longer produce a simple tri-diagonal matrix. Hermiticity is needed for the appearance of a tri-diagonal form as we saw in the previous section on the Lanczos iteration scheme.

Let $|1\rangle = \sigma_1^x$, then assuming we have found the orthonormal basis vectors $|n\rangle, |n-1\rangle, \dots$, we find $|n+1\rangle$

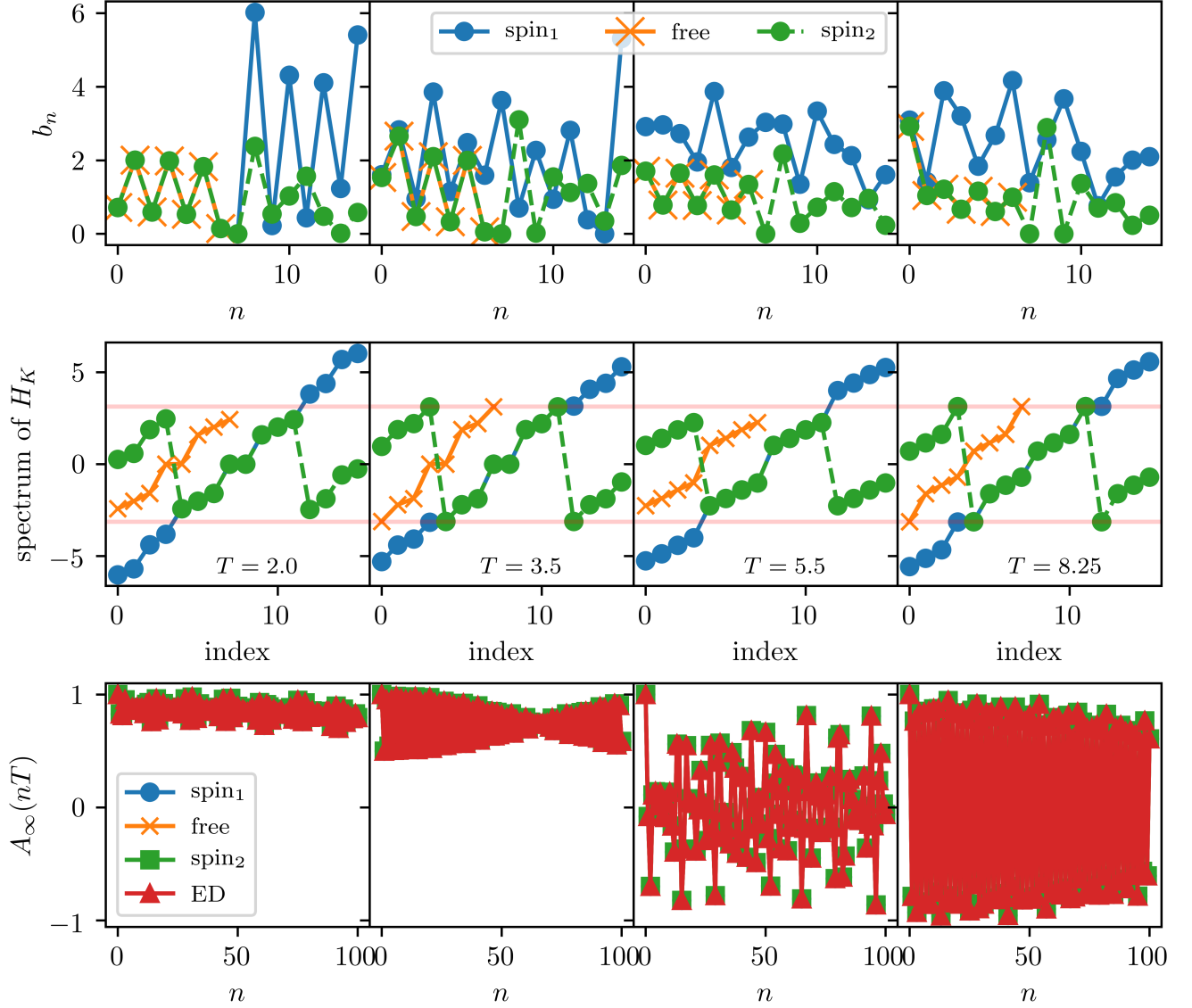


FIG. 4. Exploring the difference between the spin basis and the Majorana basis for the binary drive with $g = 0.3$ and $L = 4$. All rows, from left to right $T = 2.0, 3.5, 5.5, 8.25$. These correspond respectively to SZM, SZM-SPM, trivial, and SPM phases. Top rows show the b_n s for the Majorana basis (labeled as “free”), and the two spin bases (labeled as $\text{spin}_{1,2}$). Middle rows show the spectra of the corresponding Krylov Hamiltonians. The bottom rows plot A_∞ obtained from performing the time-evolution using the three different Krylov Hamiltonians. The red data labeled as “ED” in the bottom row is A_∞ from ED.

by time evolving it, and projecting out the overlaps with the known basis vectors. Thus we have

$$\begin{aligned} |n+1'\rangle &= W|n\rangle - \sum_{l=1}^n |l\rangle(l|W|n) \\ &= W|n\rangle - \sum_{l=1}^n w_{l,n}|l\rangle \end{aligned} \quad (36)$$

$$= \left[1 - \sum_{l=1}^n |l\rangle(l| \right] W|n\rangle = P_n W|n\rangle. \quad (37)$$

Above $w_{l,n} = (l|W|n)$ and $P_n = 1 - \sum_{l=1}^n |l\rangle(l|$ projects

out overlaps with the previously calculated basis vectors. Following this we normalize $|n+1'\rangle$,

$$|n+1\rangle = \frac{|n+1'\rangle}{\sqrt{(n+1'|n+1')}}. \quad (38)$$

We note that

$$(n+1'|n+1') = (n+1'|P_n W|n) = (n+1'|W|n), \quad (39)$$

because $(n+1'|l) = 0$ for $l = 1 \dots n$ due to the projector P_n . Using Eq. (38) the above becomes

$$(n+1'|n+1') = \sqrt{(n+1'|n+1')}(n+1|W|n), \quad (40)$$

implying that

$$\sqrt{(n+1'|n+1')} = (n+1|W|n) = w_{n+1,n}. \quad (41)$$

Thus we start with $|1\rangle$, find $W|1\rangle$ and $(1|W|1) = w_{1,1}$. Following this we find the unnormalized $|2'\rangle = W|1\rangle - w_{1,1}|1\rangle$. Then we determine the coefficient $w_{2,1}$ from $(2'|2') = w_{2,1}^2$. This first step fills in the first two rows of the first column of W in the Arnoldi basis.

Flipping Eq. (36) around, we have

$$W|n\rangle = w_{n+1,n}|n+1\rangle + \sum_{l=1}^n w_{l,n}|l\rangle. \quad (42)$$

Thus as we iterate through this Arnoldi algorithm, we will find that W has the following upper Hessenberg form

$$W = \begin{pmatrix} w_{1,1} & w_{1,2} & \dots \\ w_{2,1} & w_{2,2} & \dots \\ 0 & w_{3,2} & \dots \\ \vdots & \vdots & \ddots \end{pmatrix}. \quad (43)$$

In particular an upper Hessenberg matrix is a square matrix whose elements $w_{i,j} = 0$ for $i > j + 1$, i.e, it is a matrix whose elements are zero below the first sub-diagonal [38]. In addition, when the seed operator is Hermitian, all the elements of W are real because under time-evolution a Hermitian operator stays Hermitian, with the matrix elements of W simply denoting the weight of different Hermitian operators at a particular step in the iterative procedure. Typically the structure of W is such that the elements on the first sub-diagonal are dominant. These elements besides measuring the norm of the operators (see Eq. (41)), also measure how much the operator is spreading into new parts of the Krylov subspace. In contrast, all other elements of W are simply the overlap of the new operator generated at each iteration, with previous elements of the Krylov subspace. Moreover, the further an element is from the first sub-diagonal, the smaller it is. This observation will be handy later when we derive analytic expressions for W .

The autocorrelation function in terms of W now has the form

$$A_\infty(nT) = (1|W^n|1). \quad (44)$$

Just as for \mathcal{L} , the iteration must be cut short after N steps. Due to the truncation, the resulting W will not be unitary. As we will show later in the context of ASZMs and ASPMs, as long as N is sufficiently large, the truncated W does well in reproducing the dynamics. The success of the approximation is a good indication that if the edge modes are sufficiently localized at the edge of the Krylov chain, the truncation scheme does not affect the physics.

We note that for the last state $|N\rangle$ we have,

$$W|N\rangle = \sum_{l=1}^N w_{l,N}|l\rangle + w_{N+1,N}|N+1\rangle, \quad (45)$$

and by stopping at $|N\rangle$, we are making some form of a Markov approximation at a rate of $w_{N+1,N}$. Thus we expect almost all operator dynamics produced by truncated W to eventually decay.

A. Strong modes in limiting cases

We now discuss the form of the W matrix for some analytically tractable limiting cases. These limits were already discussed in previous sections in the context of the matrix K in Eq. (9).

- $Tg = (2n+1)\pi$, T arbitrary: For this case $e^{-iTgH_z/2} \propto \mathcal{D}$, thus $U^\dagger \sigma_1^x U = \mathcal{D} \sigma_1^x \mathcal{D} = -\sigma_1^x$, and a SPM exists, whereas there is no SZM. The first step of the Arnoldi iteration is $|1\rangle = \sigma_1^x$ and the next state is

$$|2'\rangle = W|1\rangle = -|1\rangle. \quad (46)$$

Thus the Krylov subspace terminates after the first basis vector $|1\rangle = \sigma_1^x$, and W is a "matrix" with a single element, -1 .

- $Tg = (2n)\pi$, T arbitrary: For this case $e^{-iTgH_z/2} \propto 1$ and $U^\dagger \sigma_1^x U = \sigma_1^x$. We have a SZM, but no SPM. Following the same steps as in the previous case, it is clear that $W = 1$.
- $T = (2n+1)\pi$, Tg arbitrary: We now have $e^{-iTgH_{xx}/2} \propto \sigma_1^x \sigma_L^x$, with $e^{-iTgH_z/2} = \prod_l [\cos(Tg/2) - i\sigma_l^z \sin(Tg/2)]$. For this case Eq. (11) holds. We now construct the Krylov subspace for σ_1^x . Beginning with $|1\rangle = \sigma_1^x$, we have using Eq. (11)

$$W|1\rangle = \cos(Tg)\sigma_1^x - \sin(Tg)\sigma_1^y, \quad (47)$$

giving,

$$|2'\rangle = W|1\rangle - \cos(Tg)|1\rangle = -\sin(Tg)\sigma_1^y. \quad (48)$$

After normalization we obtain

$$|2\rangle = -\sigma_1^y. \quad (49)$$

Moreover, again using Eq. (11), we can see that $W|2\rangle$ will be a linear combination of $|1\rangle, |2\rangle$, and in particular

$$W = \begin{pmatrix} \cos(Tg) & |\sin(Tg)| \\ |\sin(Tg)| & -\cos(Tg) \end{pmatrix}, \quad (50)$$

which corresponds to having both a SZM and a SPM as the eigenvalues of W are ± 1 .

- $T = 2n\pi$ and Tg arbitrary: For this case we have $e^{-iTgH_{xx}/2} \propto 1$ and the time-evolution is given

by Eq. (12). Carrying out the same steps as before one finds that the Krylov subspace for σ_1^x is 2 dimensional with

$$W = \begin{pmatrix} \cos(Tg) & -|\sin(Tg)| \\ |\sin(Tg)| & \cos(Tg) \end{pmatrix}. \quad (51)$$

Thus the eigenvalues are pure phases that do not equal ± 1 , unless $Tg = n\pi$, where n is an integer. When $n \in \text{even}$, we have a SZM, and when $n \in \text{odd}$, we have a SPM.

V. ARNOLDI ITERATION FOR THE BINARY DRIVE

In this section we present the analytic form of W for the binary drive, and discuss it for the same limiting

cases as the ones for which K was constructed in Section II. Recall that for the binary drive, we can work in the Majorana basis where a chain of length L requires diagonalizing the problem in a reduced Hilbert space of size $2L$.

$$W = \begin{pmatrix} c_1 & -s_1 c_2 & s_2 s_1 c_1 & -s_2 s_1^2 c_2 & s_2^2 s_1^2 c_1 & -s_2^2 s_1^3 c_2 & s_2^3 s_1^3 c_1 & -s_2^3 s_1^4 c_2 \\ s_1 & c_2 c_1 & -s_2 c_1^2 & s_1 c_1 s_2 c_2 & -s_2^2 s_1 c_1^2 & s_2^2 s_1^2 c_2 c_1 & -s_2^3 s_1^2 c_1^2 & s_2^3 s_1^3 c_1 \\ 0 & s_2 & c_2 c_1 & -s_1 c_2^2 & s_1 c_1 s_2 c_2 & -s_2 s_1^2 c_2^2 & s_2^2 s_1^2 c_2 c_1 & -s_2^2 s_1^3 c_2 \\ 0 & 0 & s_1 & c_2 c_1 & -s_2 c_1^2 & s_1 c_1 s_2 c_2 & -s_2^2 s_1 c_1^2 & s_2^2 s_1^2 c_1 \\ 0 & 0 & 0 & s_2 & c_2 c_1 & -s_1 c_2^2 & s_1 c_1 s_2 c_2 & -s_2 s_1^2 c_2 \\ 0 & 0 & 0 & 0 & s_1 & c_2 c_1 & -s_2 c_1^2 & s_1 c_1 s_2 \\ 0 & 0 & 0 & 0 & 0 & s_2 & c_2 c_1 & -s_1 c_2 \\ 0 & 0 & 0 & 0 & 0 & 0 & s_1 & c_1 \end{pmatrix}, \quad (52)$$

where $c_{1,2}, s_{1,2}$ were defined in Eq. (8). We discuss the structure of W as it will help us make further approximations. Firstly since W is unitary, its rows and columns form an orthonormal basis. Secondly, for even rows, starting on the column corresponding to the sub-diagonal, we have

$$\{s_1, c_1 c_2, -s_2 c_1^2, (s_1 s_2) c_1 c_2, -(s_1 s_2) s_2 c_1^2, \dots, (s_1 s_2)^n (c_1 c_2), (s_1 s_2)^n (-s_2 c_1^2), \dots\}. \quad (53)$$

Thirdly, for odd rows, starting on the column corresponding to the sub-diagonal, we have

$$\{s_2, c_1 c_2, -s_1 c_2^2, (s_1 s_2) c_1 c_2, -(s_1 s_2) s_1 c_2^2, \dots, (s_1 s_2)^n (c_1 c_2), (s_1 s_2)^n (-s_1 c_2^2), \dots\}. \quad (54)$$

The rows and columns at the edge of the matrix can be determined from using the above rules and then dividing by c_2 . This also ensures orthonormality of the rows and columns. In what follows we will further explore W , and in particular $\ln W$ for limiting cases that give SZMs and SPMs. The reason for exploring $\ln W$ is that it has a Hamiltonian description, and therefore the topological properties can be more easily discerned.

A. $\ln W$ for $gT \ll 1$, $T \ll 1$: SZM phase

First let us consider the case when $gT \ll 1$. For this case we have s_2, c_2 arbitrary, and $s_1 \ll 1, c_1 \approx 1$. Truncating the W matrix in Eq. (52) to terms of $O(s_1)$ we have

$$W = \begin{pmatrix} 1 & -s_1 c_2 & s_2 s_1 & 0 & 0 & 0 & 0 & 0 \\ s_1 & c_2 & -s_2 & s_1 s_2 c_2 & -s_2^2 s_1 & 0 & 0 & 0 \\ 0 & s_2 & c_2 & -s_1 c_2^2 & s_1 s_2 c_2 & 0 & 0 & 0 \\ 0 & 0 & s_1 & c_2 & -s_2 & s_1 s_2 c_2 & -s_2^2 s_1 & 0 \\ 0 & 0 & 0 & s_2 & c_2 & -s_1 c_2^2 & s_1 s_2 c_2 & 0 \\ 0 & 0 & 0 & 0 & s_1 & c_2 & -s_2 & s_1 s_2 \\ 0 & 0 & 0 & 0 & 0 & s_2 & c_2 & -s_1 c_2 \\ 0 & 0 & 0 & 0 & 0 & 0 & s_1 & 1 \end{pmatrix} + O(s_1^2) = W_0 + \delta W, \quad (55)$$

$$W_0 = \begin{pmatrix} 1 & 0 & 0 & 0 & 0 & 0 & 0 & 0 \\ 0 & c_2 & -s_2 & 0 & 0 & 0 & 0 & 0 \\ 0 & s_2 & c_2 & 0 & 0 & 0 & 0 & 0 \\ 0 & 0 & 0 & c_2 & -s_2 & 0 & 0 & 0 \\ 0 & 0 & 0 & s_2 & c_2 & 0 & 0 & 0 \\ 0 & 0 & 0 & 0 & 0 & c_2 & -s_2 & 0 \\ 0 & 0 & 0 & 0 & 0 & s_2 & c_2 & 0 \\ 0 & 0 & 0 & 0 & 0 & 0 & 0 & 1 \end{pmatrix} = W(gT = 0), \quad (56)$$

$$\delta W = \begin{pmatrix} 0 & -s_1 c_2 & s_2 s_1 & 0 & 0 & 0 & 0 & 0 \\ s_1 & 0 & 0 & s_1 s_2 c_2 & -s_2^2 s_1 & 0 & 0 & 0 \\ 0 & 0 & 0 & -s_1 c_2^2 & s_1 s_2 c_2 & 0 & 0 & 0 \\ 0 & 0 & s_1 & 0 & 0 & s_1 s_2 c_2 & -s_2^2 s_1 & 0 \\ 0 & 0 & 0 & 0 & 0 & -s_1 c_2^2 & s_1 s_2 c_2 & 0 \\ 0 & 0 & 0 & 0 & s_1 & 0 & 0 & s_1 s_2 \\ 0 & 0 & 0 & 0 & 0 & 0 & 0 & -s_1 c_2 \\ 0 & 0 & 0 & 0 & 0 & 0 & s_1 & 0 \end{pmatrix}. \quad (57)$$

Above $W_0 = W(gT = 0)$. If in addition we impose $T \ll 1$ which is equivalent to $s_2 \ll 1$, the matrices W_0 and δW commute if terms of $O(s_1 s_2), O(s_1^2), O(s_2^2)$ and higher are dropped. Using, Eq. (17) we find the following expressing to first order in s_1 and T

$$i \ln [W] \approx \begin{pmatrix} 0 & -is_1 & 0 & 0 & 0 & 0 & 0 & 0 \\ is_1 & 0 & -iT & 0 & 0 & 0 & 0 & 0 \\ 0 & iT & 0 & -is_1 & 0 & 0 & 0 & 0 \\ 0 & 0 & is_1 & 0 & -iT & 0 & 0 & 0 \\ 0 & 0 & 0 & iT & 0 & -is_1 & 0 & 0 \\ 0 & 0 & 0 & 0 & is_1 & 0 & -iT & 0 \\ 0 & 0 & 0 & 0 & 0 & iT & 0 & -is_1 \\ 0 & 0 & 0 & 0 & 0 & 0 & is_1 & 0 \end{pmatrix}. \quad (58)$$

This should be compared with $i \ln K$ in Eq. (18). Both $i \ln W$ and $i \ln K$ represent Floquet Hamiltonians that are effectively SSH models with topologically non-trivial sign of the dimerization for $|s_1| < T$. Thus a zero mode is guaranteed.

B. $\ln W$ for $gT \approx \pi$, $T \ll 1$: SPM phase

Let us first consider $gT \approx \pi$ where $s_1 \ll 1$ and $c_1 = -1$. Truncating W in Eq. (52) to $O(s_1)$ we obtain

$$W = \begin{pmatrix} -1 & -s_1 c_2 & -s_2 s_1 & 0 & 0 & 0 & 0 & 0 \\ s_1 & -c_2 & -s_2 & -s_1 s_2 c_2 & -s_2^2 s_1 & 0 & 0 & 0 \\ 0 & s_2 & -c_2 & -s_1 c_2^2 & -s_1 s_2 c_2 & 0 & 0 & 0 \\ 0 & 0 & s_1 & -c_2 & -s_2 & -s_1 s_2 c_2 & -s_2^2 s_1 & 0 \\ 0 & 0 & 0 & s_2 & -c_2 & -s_1 c_2^2 & -s_1 s_2 c_2 & 0 \\ 0 & 0 & 0 & 0 & s_1 & -c_2 & -s_2 & -s_1 s_2 \\ 0 & 0 & 0 & 0 & 0 & s_2 & -c_2 & -s_1 c_2 \\ 0 & 0 & 0 & 0 & 0 & 0 & s_1 & -1 \end{pmatrix} + O(s_1^2) = W_0 + \delta W, \quad (59)$$

$$W_0 = W(gT = \pi) = - \begin{pmatrix} 1 & 0 & 0 & 0 & 0 & 0 & 0 & 0 \\ 0 & c_2 & s_2 & 0 & 0 & 0 & 0 & 0 \\ 0 & -s_2 & c_2 & 0 & 0 & 0 & 0 & 0 \\ 0 & 0 & 0 & c_2 & s_2 & 0 & 0 & 0 \\ 0 & 0 & 0 & -s_2 & c_2 & 0 & 0 & 0 \\ 0 & 0 & 0 & 0 & 0 & c_2 & s_2 & 0 \\ 0 & 0 & 0 & 0 & 0 & -s_2 & c_2 & 0 \\ 0 & 0 & 0 & 0 & 0 & 0 & 0 & 1 \end{pmatrix}, \quad (60)$$

$$\delta W = \begin{pmatrix} 0 & -s_1 c_2 & -s_2 s_1 & 0 & 0 & 0 & 0 & 0 \\ s_1 & 0 & 0 & -s_1 s_2 c_2 & -s_2^2 s_1 & 0 & 0 & 0 \\ 0 & 0 & 0 & -s_1 c_2^2 & -s_1 s_2 c_2 & 0 & 0 & 0 \\ 0 & 0 & s_1 & 0 & 0 & -s_1 s_2 c_2 & -s_2^2 s_1 & 0 \\ 0 & 0 & 0 & 0 & 0 & -s_1 c_2^2 & -s_1 s_2 c_2 & 0 \\ 0 & 0 & 0 & 0 & s_1 & 0 & 0 & -s_1 s_2 \\ 0 & 0 & 0 & 0 & 0 & 0 & 0 & -s_1 c_2 \\ 0 & 0 & 0 & 0 & 0 & 0 & s_1 & 0 \end{pmatrix}.$$

If we now also assume $T \ll 1$ which is equivalent to $s_2 \ll 1$, then W_0 and δW commute if terms of $O(s_1 s_2)$, $O(s_1^2)$, $O(s_2^2)$ and higher are dropped. Performing the expansion in Eq. (17) we find, to first order in s_1 and T

$$i \ln [W] \approx \pm \pi + \begin{pmatrix} 0 & i s_1 & 0 & 0 & 0 & 0 & 0 & 0 \\ -i s_1 & 0 & iT & 0 & 0 & 0 & 0 & 0 \\ 0 & -iT & 0 & i s_1 & 0 & 0 & 0 & 0 \\ 0 & 0 & -i s_1 & 0 & iT & 0 & 0 & 0 \\ 0 & 0 & 0 & -iT & 0 & i s_1 & 0 & 0 \\ 0 & 0 & 0 & 0 & -i s_1 & 0 & iT & 0 \\ 0 & 0 & 0 & 0 & 0 & -iT & 0 & i s_1 \\ 0 & 0 & 0 & 0 & 0 & 0 & -i s_1 & 0 \end{pmatrix}. \quad (61)$$

Comparing the above to Eq. (22) we find that the two Floquet Hamiltonians are similar. Moreover, the presence of a SPM is guaranteed because both $i \ln W$ and $i \ln K$ are topologically non-trivial SSH models, with a constant shift of π which ensures that the zero mode of the SSH model is shifted in energy by π .

C. $\ln W$ for $T \approx \pi$: SZM-SPM phase

Let us consider the case $T \approx \pi$. For this case we have $c_2 \approx -1, s_2 \ll 1$ while c_1, s_1 are arbitrary. Truncating Eq. (52) to $O(s_2)$ we obtain

$$\begin{aligned}
 W &= \begin{pmatrix} c_1 & s_1 & s_1 s_2 c_1 & s_1^2 s_2 & 0 & 0 & 0 & 0 \\ s_1 & -c_1 & -s_2 c_1^2 & -s_1 s_2 c_1 & 0 & 0 & 0 & 0 \\ 0 & s_2 & -c_1 & -s_1 & -s_1 s_2 c_1 & -s_1^2 s_2 & 0 & 0 \\ 0 & 0 & s_1 & -c_1 & -s_2 c_1^2 & -s_1 s_2 c_1 & 0 & 0 \\ 0 & 0 & 0 & s_2 & -c_1 & -s_1 & -s_1 s_2 c_1 & s_1^2 s_2 \\ 0 & 0 & 0 & 0 & s_1 & -c_1 & -s_2 c_1^2 & s_1 s_2 c_1 \\ 0 & 0 & 0 & 0 & 0 & s_2 & -c_1 & s_1 \\ 0 & 0 & 0 & 0 & 0 & 0 & s_1 & c_1 \end{pmatrix} + O(s_2^2) = W_0 + \delta W, \quad (62) \\
 W_0 = W(T = \pi) &= \begin{pmatrix} c_1 & s_1 & 0 & 0 & 0 & 0 & 0 & 0 \\ s_1 & -c_1 & 0 & 0 & 0 & 0 & 0 & 0 \\ 0 & 0 & -c_1 & -s_1 & 0 & 0 & 0 & 0 \\ 0 & 0 & s_1 & -c_1 & 0 & 0 & 0 & 0 \\ 0 & 0 & 0 & 0 & -c_1 & -s_1 & 0 & 0 \\ 0 & 0 & 0 & 0 & s_1 & -c_1 & 0 & 0 \\ 0 & 0 & 0 & 0 & 0 & 0 & -c_1 & s_1 \\ 0 & 0 & 0 & 0 & 0 & 0 & s_1 & c_1 \end{pmatrix} \\
 &= \begin{pmatrix} \pm i e^{\mp i \frac{\pi}{2} (c_1 \sigma_z + s_1 \sigma_x)} & 0 & 0 & 0 & 0 & 0 & 0 & 0 \\ 0 & 0 & 0 & 0 & 0 & 0 & 0 & 0 \\ 0 & 0 & -e^{iT \sigma_y} & 0 & 0 & 0 & 0 & 0 \\ 0 & 0 & 0 & 0 & 0 & 0 & 0 & 0 \\ 0 & 0 & 0 & 0 & -e^{iT \sigma_y} & 0 & 0 & 0 \\ 0 & 0 & 0 & 0 & 0 & 0 & 0 & 0 \\ 0 & 0 & 0 & 0 & 0 & 0 & \pm i e^{\mp i \frac{\pi}{2} (-c_1 \sigma_z + s_1 \sigma_x)} & 0 \end{pmatrix}, \\
 \delta W &= \begin{pmatrix} 0 & 0 & s_1 s_2 c_1 & s_1^2 s_2 & 0 & 0 & 0 & 0 \\ 0 & 0 & -s_2 c_1^2 & -s_1 s_2 c_1 & 0 & 0 & 0 & 0 \\ 0 & s_2 & 0 & 0 & -s_1 s_2 c_1 & -s_1^2 s_2 & 0 & 0 \\ 0 & 0 & 0 & 0 & -s_2 c_1^2 & -s_1 s_2 c_1 & 0 & 0 \\ 0 & 0 & 0 & s_2 & 0 & 0 & -s_1 s_2 c_1 & s_1^2 s_2 \\ 0 & 0 & 0 & 0 & 0 & 0 & -s_2 c_1^2 & s_1 s_2 c_1 \\ 0 & 0 & 0 & 0 & 0 & s_2 & 0 & 0 \\ 0 & 0 & 0 & 0 & 0 & 0 & 0 & 0 \end{pmatrix}. \quad (63)
 \end{aligned}$$

At this stage we simply discuss the Floquet Hamiltonian $\ln(W_0)$,

$$\ln[W_0] \approx \begin{pmatrix} \ln \left[\pm i e^{\mp i \frac{\pi}{2} (c_1 \sigma_z + s_1 \sigma_x)} \right] & 0 & 0 & 0 & 0 & 0 & 0 & 0 \\ 0 & 0 & 0 & 0 & 0 & 0 & 0 & 0 \\ 0 & 0 & \ln \left[-e^{iT \sigma_y} \right] & 0 & 0 & 0 & 0 & 0 \\ 0 & 0 & 0 & 0 & 0 & 0 & 0 & 0 \\ 0 & 0 & 0 & 0 & \ln \left[-e^{iT \sigma_y} \right] & 0 & 0 & 0 \\ 0 & 0 & 0 & 0 & 0 & 0 & 0 & 0 \\ 0 & 0 & 0 & 0 & 0 & 0 & \ln \left[\pm i e^{\mp i \frac{\pi}{2} (-c_1 \sigma_z + s_1 \sigma_x)} \right] & 0 \end{pmatrix}. \quad (64)$$

Thus we see that $i \ln(W_0)$, for these parameters, has a complex edge structure represented by the 2×2 block in the upper and lower diagonals. These edge modes are completely decoupled from a bulk which has a dimerization of a topologically non-trivial SSH model. Deviating from this exactly solvable limit will couple the edge modes weakly to the bulk states, and will also generate longer range hopping. However, these edge modes are protected as long as the bulk gap remains non-zero.

VI. LIFETIME OF EDGE MODES FROM THE ARNOLDI ALGORITHM

In this section we construct the approximate edge mode and derive its lifetime for the most general W matrix whose upper-Hessenberg form is highlighted in Eq. (43). The results derived here hold for the free and the interacting cases. Recall that for the free system we have a SZM and/or a SPM. These acquire a lifetime due to finite size effects, i.e, their lifetime scales exponentially in the system size L . On the other hand, when the interactions are non-zero, the edge modes acquire a system-size independent lifetime provided the system size is large enough. For small system sizes, there is not much of a difference between strong modes and almost strong modes as both have lifetimes that grow exponentially with system size.

We denote edge modes of W , both exact and approximate, as $|\psi_{0,\pi}\rangle$, where the subscript indicates whether it is a zero mode or a π -mode. We then argue that the lifetime $\gamma_{0,\pi}^{-1}$ of the edge mode is well approximated by the expression

$$e^{-\gamma_{0,\pi}} = |\langle\psi_{0,\pi}|W|\psi_{0,\pi}\rangle|, \quad (65)$$

where $\gamma_{0,\pi}$ is in dimensionless units. We will present numerical evidence for this. It is straightforward to see that when $|\psi_{0,\pi}\rangle$ are exact edge modes, $|\langle\psi_{0,\pi}|W|\psi_{0,\pi}\rangle| = 1$ and the decay rate $\gamma_{0,\pi} = 0$. We will apply the formula to the case where we have quasi-stable edge modes, so that $|\langle\psi_{0,\pi}|W|\psi_{0,\pi}\rangle| < 1$, resulting in a non-zero decay rate.

We solve for the edge modes by determining the left eigenvectors of W ,

$$\langle\psi_{0,\pi}|W = \tilde{\lambda}\langle\psi_{0,\pi}|, \quad (66)$$

with $\tilde{\lambda} = 1$ for $\langle\psi_0|$ and $\tilde{\lambda} = -1$ for $\langle\psi_\pi|$. Essentially this allows us to work from the first site and iterate into the bulk. We denote the elements of $\langle\psi_{0,\pi}|$ by ψ_i where the subscript i is the site index. The first step involves the inner product of the left eigenvector with the first column of $W - \tilde{\lambda}$ which gives

$$\psi_1 = 1, \quad (67)$$

$$\psi_2 = -\left(\frac{w_{1,1} - \tilde{\lambda}}{w_{2,1}}\right). \quad (68)$$

Above we set $\psi_1 = 1$ as we are interested in an edge mode. The inner product of the left eigenvector onto the second column of the matrix $W - \tilde{\lambda}$ gives

$$\psi_3 = -\frac{1}{w_{3,2}} \left[(w_{2,2} - \tilde{\lambda})\psi_2 + w_{1,2}\psi_1 \right]. \quad (69)$$

The pattern is clear for the rest of the eigenvector components,

$$\psi_{n+1} = -\frac{1}{w_{n+1,n}} \left[(w_{n,n} - \tilde{\lambda})\psi_n + \sum_{i=1}^{n-1} w_{i,n}\psi_i \right], \quad (70)$$

with a final normalization step at the end of the calculation.

We now rewrite Eq. (70) as follows as it will be helpful later

$$\sum_{i=1}^{n-1} \psi_i w_{i,n} = -\psi_{n+1} w_{n+1,n} - (w_{n,n} - \tilde{\lambda})\psi_n. \quad (71)$$

Since all the elements of W are real, the components ψ_i of the edge mode are also real. We now set out to compute the right hand side of Eq. (65). It is straightforward to see that

$$\langle\psi_{0,\pi}|W|\psi_{0,\pi}\rangle = \sum_{k=1}^{N-1} \left[\psi_{k+1} w_{k+1,k} + \psi_k w_{k,k} + \sum_{m=1}^{k-1} \psi_m w_{m,k} \right] \psi_k + \sum_{m=1}^N \psi_m w_{m,N} \psi_N \quad (72)$$

$$= \sum_{k=1}^{N-1} \left[\psi_{k+1} w_{k+1,k} + \psi_k w_{k,k} + \left(-\psi_{k+1} w_{k+1,k} - (w_{k,k} - \tilde{\lambda})\psi_k \right) \right] \psi_k + \sum_{m=1}^N \psi_m w_{m,N} \psi_N \quad (73)$$

$$= \sum_{k=1}^{N-1} \tilde{\lambda} \psi_k^2 + \sum_{m=1}^N \psi_m w_{m,N} \psi_N \quad (74)$$

$$= \tilde{\lambda} \left[\sum_{k=1}^N \psi_k^2 + \tilde{\lambda} \sum_{m=1}^N \psi_m w_{m,N} \psi_N - \psi_N^2 \right]. \quad (75)$$

In the second equality above we have used Eq. (71) to simplify the expression.

We normalize $\psi_{0,\pi} \rightarrow \psi_{0,\pi}/N_{0,\pi}$ and use that $|\tilde{\lambda}| = 1$

to obtain

$$|\langle\psi_{0,\pi}|W|\psi_{0,\pi}\rangle| = 1 + \frac{\tilde{\lambda}}{N_{0,\pi}^2} \sum_{m=1}^N \psi_m w_{m,N} \psi_N - \frac{\psi_N^2}{N_{0,\pi}^2}. \quad (76)$$

Using Eq. (65), we identify the decay rate from Taylor expanding the left hand side of the same equation to obtain

$$\gamma_{0,\pi} \approx \frac{\psi_N^2}{N_{0,\pi}^2} - \frac{\tilde{\lambda}}{N_{0,\pi}^2} \sum_{m=1}^N \psi_m w_{m,N} \psi_N. \quad (77)$$

We cannot proceed further without making approximations to W or to ψ . As it stands, Eq. (77) agrees well with the quantity $\ln |\langle \psi_{0,\pi} | W | \psi_{0,\pi} \rangle|$ which was how the decay-rate was defined in Eq. (65). We give evidence of this in the next section. Empirically, we also find that the second term in Eq. (77) is often much smaller than the first, thus we can approximate the expression for the decay rate even further as

$$\gamma_{0,\pi} \approx \psi_N^2. \quad (78)$$

Above we are explicitly working with the normalized wavefunction and therefore we have dropped the factor of $N_{0,\pi}^2$. Thus the decay rate is the probability of the edge mode to be located at the site N . Recall that N is the dimension of the W matrix. For the free case, if $N = 2L$, this exhausts the Hilbert space. For the interacting problem N has to be very large $\approx e^{2L}$ in order to exhaust the Hilbert space. Thus when working with interacting systems, we will always be truncating W . However as long as this truncation occurs for an N which is large enough, and the quasi-stable edge-mode is sufficiently localized at the edge, the decay rate $\gamma_{0,\pi}$, and therefore the probability of finding the particle at site N , will be independent of N (for a given system size L).

VII. KRYLOV SUBSPACE WITH INTERACTIONS

We now consider the interacting example by modifying the binary drive in Eq. (1) into a ternary drive where the third part of the drive breaks the free fermion nature of the problem. Specifically we study

$$U = e^{-i\frac{T}{2}J_z H_{zz}} e^{-i\frac{T}{2}J_x H_{xx}} e^{-i\frac{T}{2}g H_z}, \quad (79)$$

where the interacting part is

$$H_{zz} = \sum_{i=1}^{L-1} \sigma_i^z \sigma_{i+1}^z. \quad (80)$$

The above drive was studied in detail in [22, 37], and it was found that the SZMs and SPMs get modified to ASZMs and ASPMs where the latter are characterized by a system size independent lifetime, for sufficiently large system sizes. Moreover, this lifetime is still very long as compared to the time needed for the bulk of the system to heat to infinite temperature. In this section we outline how the ASZM and ASPM manifest in Krylov subspaces. We first discuss their appearance in the Lanczos iteration scheme, and then we discuss their appearance in the Arnoldi iteration scheme.

A. Krylov subspace from Lanczos iteration

We evaluate U in Eq. (79) by ED, and then take its logarithm in order to arrive at the Floquet Hamiltonian

$$H_F = \frac{i}{T} \ln(U). \quad (81)$$

Then, as outlined in Section III, we apply the iterative Lanczos scheme with the seed operator σ_1^x , obtaining the Krylov Hamiltonian Eq. (30). The results for the b_n s are shown in Fig. 5, while the corresponding spectra are shown in Fig. 6. In these figures we hold J_z fixed to $J_z = 0.01$, while g is taken to have the same value as for the binary drive discussed in previous sections, namely $g = 0.3$. In addition we choose T to takes four different values, one corresponding to a high-frequency drive $T < 1$, while the remaining three are for a low frequency drive $T > 1$. For the high frequency drive we choose $T = 0.5$ (an ASZM phase), while for the low frequency drive we choose $T = 2.0$ (an ASZM phase), $T = 3.5$, (an ASZM-ASPM phase) and $T = 8.25$ (an ASPM phase). The three cases of the low frequency drive and for $J_z = 0$ i.e, the binary drive were already presented in the previous sections.

The b_n s for the case of the high frequency drive, $T = 0.5$, are shown in the top left panel of Fig. 5, and the corresponding spectrum is shown in the first panel of Fig. 6. This case hosts a ASZM which can be interpreted as the ASZM of the static spin chain [16, 17] only modestly modified by the drive. In fact, the b_n s do look very similar to those discussed for the static chain in that there is a spatially inhomogeneous dimerization superimposed on a non-zero slope [16, 17]. The value of the slope increases with increasing J_z for the static spin chain. In the absence of dimerization, and the presence of an average slope i.e, $b_n \propto n$, one has chaotic operator spreading [33–36]. The dimerization on the other hand, prevents the edge operator from spreading. This is consistent with our observation for the free case where there is no slope, but only a topologically non-trivial dimerization (see Fig. 2).

Eventually the b_n s for the interacting high frequency case, and also that of the static spin chain, stop growing with n , and reach a plateau representing a metallic bulk. The onset of the plateau shifts to larger n as the system size L increases. In addition to this behavior, the overall dimerization decreases with increasing J_z [16, 17, 37]. The influence of a decreasing dimerization ultimately terminating into a metallic bulk has the effect of causing the ASZM to finally decay, but with decay times that are non-perturbatively long in the strength of J_z [16, 17]. Due to the common features shared between the b_n s of the static chain and those of the high frequency drive, we expect the explanations for the lifetime of the ASZM should be identical for the two cases. In fact one expects that the high-frequency case is a prethermal phase of a closely related undriven model [39–43].

The spectrum of the Krylov Hamiltonian in the first

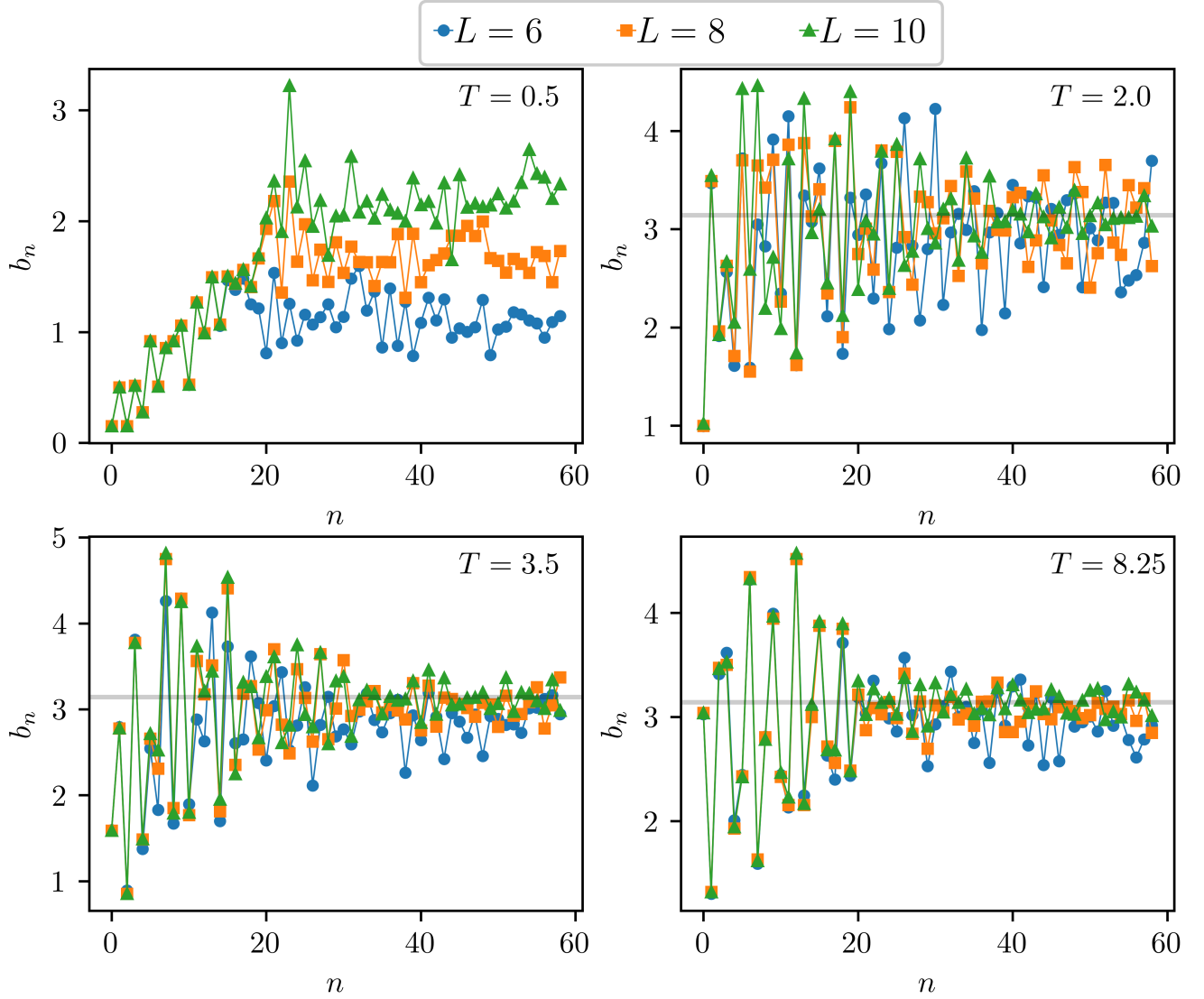


FIG. 5. b_n determined from performing Lanczos iteration on the Floquet Hamiltonian for the ternary drive Eq. (79) with $J_z = 0.01$ and $g = 0.3$. The panels correspond to an ASZM ($T = 0.5$), an ASZM ($T = 2.0$), ASZM-ASPM ($T = 3.5$) and, an ASPM ($T = 5.5$). The first ASZM occurs for a high frequency drive since $T < 1$. The b_n for the remaining three cases correspond to low frequency driving since $T > 1$. The b_n for the low frequency drive and the high frequency drive are qualitatively different. In particular, since the quasienergy spectrum is bounded, the b_n are bounded for the low frequency case, and therefore do not show the linear slope of the high-frequency case. For all cases, the bulk of the system is metallic with the dimerization vanishing, and therefore the b_n approaching a constant. For the three low frequency cases, this constant value is close to π as indicated by the horizontal black lines at $b_n = \pi$.

panel of Fig. 6 shows the existence of zero modes that are separated from bulk modes. On comparison with the binary drive (lower panel of Fig. 2), one does notice that the extent of separation between the zero modes and the bulk modes is much more for the free case than for the interacting case. In fact, the spectrum is more dense for the interacting case as the Hilbert space spanned by the operator is no longer restricted to $2L$.

The other three parameters considered in Fig. 5 and Fig. 6 all correspond to low-frequency driving $T > 1$,

with the corresponding free cases shown in Fig. 2. The figures show that the b_n s are considerably different not only from the non-interacting case, but also from the static case and the high frequency case. The main difference is that there is no overall slope on the b_n . This leads to plateaus corresponding to the metallic bulk (regions of zero dimerization) that no longer increase with increasing system size. The absence of an overall slope of the b_n s can be explained from the fact that the many-body quasi-energy spectrum is bounded between $[-\pi, \pi]$

by definition of the logarithm in Eq. (81). A bounded spectrum will produce bounded b_n s [32]. The b_n s for the low frequency cases do show a dimerization which while being spatially non-uniform, gradually decreases with increasing n . This feature is also shared by the b_n s of the static and the high frequency cases.

Let us discuss the metallic bulk of the low frequency cases. These are characterized by an absence of dimerization, $b_n = \text{constant} = b_0$, which implies a bulk dispersion of $b_0 \cos(k)$, where k denotes momenta. It is interesting to note that the lower two panels in Fig. 6, that host ASPMs, have bulk b_n s that are such that $b_0 \rightarrow \pi$ or somewhat larger. Thus the ASPMs in these figures coexist with bulk states at the same energy, and can therefore acquire a lifetime as they can now decay onto the bulk states.

In general, in the context of low-frequency driving, the specific choice of the branch of $\ln U$ taken to construct the b_n begin to matter. A general set of b_n therefore do not automatically make the physics that clear, unlike the high-frequency and static cases. In Ref. 37 it was shown that to extract relevant physics from the Lanczos scheme one has to adopt a different gauge choice where one folds the spectrum back into the FBZ, and constructs the analogous sets of b_n . This was outlined in Fig. 4 for the free case. The new b_n obtained from this gauge choice, bear a closer resemblance to the free case, and are easier to interpret.

An alternate promising approach that maps the dynamics of an interacting system to a free problem, is through the Arnoldi procedure. In this approach, by working directly with the unitary U , there are no ambiguities associated with the branches of $\ln(U)$. We discuss this case below for the interacting problem. The free case was discussed in detail in Section V.

B. Krylov subspace from the Arnoldi iteration

Section IV outlined the Arnoldi procedure. The key quantity is the unitary matrix W in Eq. (43) which has a characteristic upper Hessenberg form. The analytic expression for W and $\ln W$ for the binary drive was presented in Section V, and the lifetime of the edge mode operators for the general case including interactions was derived in Section VI. In this section we present the W matrix for the interacting problem, and apply the results for the lifetime, derived in Section VI.

Fig. 7 shows the spectrum of $i \ln W$ for the free case (top panel) and for the interacting case (bottom panel) where $J_z = 0.05$ for the interacting case. All other parameters are common between the top and bottom panels. In particular, $g = 0.3$, the system size is $L = 10$, and W is a 20×20 matrix. Thus for the free case, W is exact. However for the interacting case, W is not exact because the Hilbert space is larger than $2L$, and construction of the W matrix leads to truncation and loss of unitarity. A consequence of this is the appearance of unphysical zero

modes. This is clearly seen in the lower left-most panel of Fig. 7 which shows three zero modes, while the upper panel (free case) shows only two zero modes. Thus the truncation for the interacting case has led to the appearance of an additional spurious zero mode.

To understand why spurious zero modes can appear on truncation, let us consider a W with a simple 3×3 structure. The W have the property that the lower sub-diagonal (c.f. Eq. (41)) is the strongest as it measures the part of the operator that explores new regions of the Krylov subspace. For an ergodic system, it is natural that this element will be largest. However, an artificial truncation will cause a W of the form

$$W = \begin{pmatrix} 0 & 0 & 1 \\ 1 & 0 & 0 \\ 0 & 1 & 0 \end{pmatrix} \quad (82)$$

to become

$$W_{\text{trunc}} = \begin{pmatrix} 0 & 0 & 0 \\ 1 & 0 & 0 \\ 0 & 1 & 0 \end{pmatrix} \quad (83)$$

Now W_{trunc} has a null vector

$$W_{\text{trunc}} \begin{pmatrix} 0 \\ 0 \\ 1 \end{pmatrix} = 0 \quad (84)$$

This null vector is not shared by the untruncated W . Thus quite generally, the fact that the lower sub-diagonal is dominant in W can lead to the appearance of null vectors when the W matrix is truncated, where the null vectors have a large weight at the lower end.

We now discuss the (A)SPMs. The $\pm\pi$ modes are clearly visible on the top panel, and they are found to persist in the presence of interactions, although the edge modes are not so well separated in energy from the bulk states when interactions are present. This is expected as we now have ASPMs which will now decay into the bulk. Sometimes the mode at $-\pi$ can appear at π as seen in the lower fourth panel. This is not a spurious effect because $-\pi$ and π states are degenerate states due to the periodicity of the spectrum. However the truncation can lead to spurious effects such as the disappearance of one of the π modes as can be seen in the lower second panel.

We now turn to the computation of A_∞ and extracting the lifetime. Fig. 8 shows the autocorrelation functions for $g = 0.3$, $J_z = 0.05$ and for the same set of T as Fig. 7. The top row is for $L = 4$ while the bottom row is for $L = 8$. The blue dots are A_∞ from ED. The orange data are the A_∞ obtained from the W matrix, with the W matrix truncated to $N = 18$. We have checked that the truncation at $N = 18$ does not influence the results for the system sizes chosen ($L = 4, 8$).

The precise quantity being plotted in orange (labeled W) is Eq. (44), but with some approximations made to

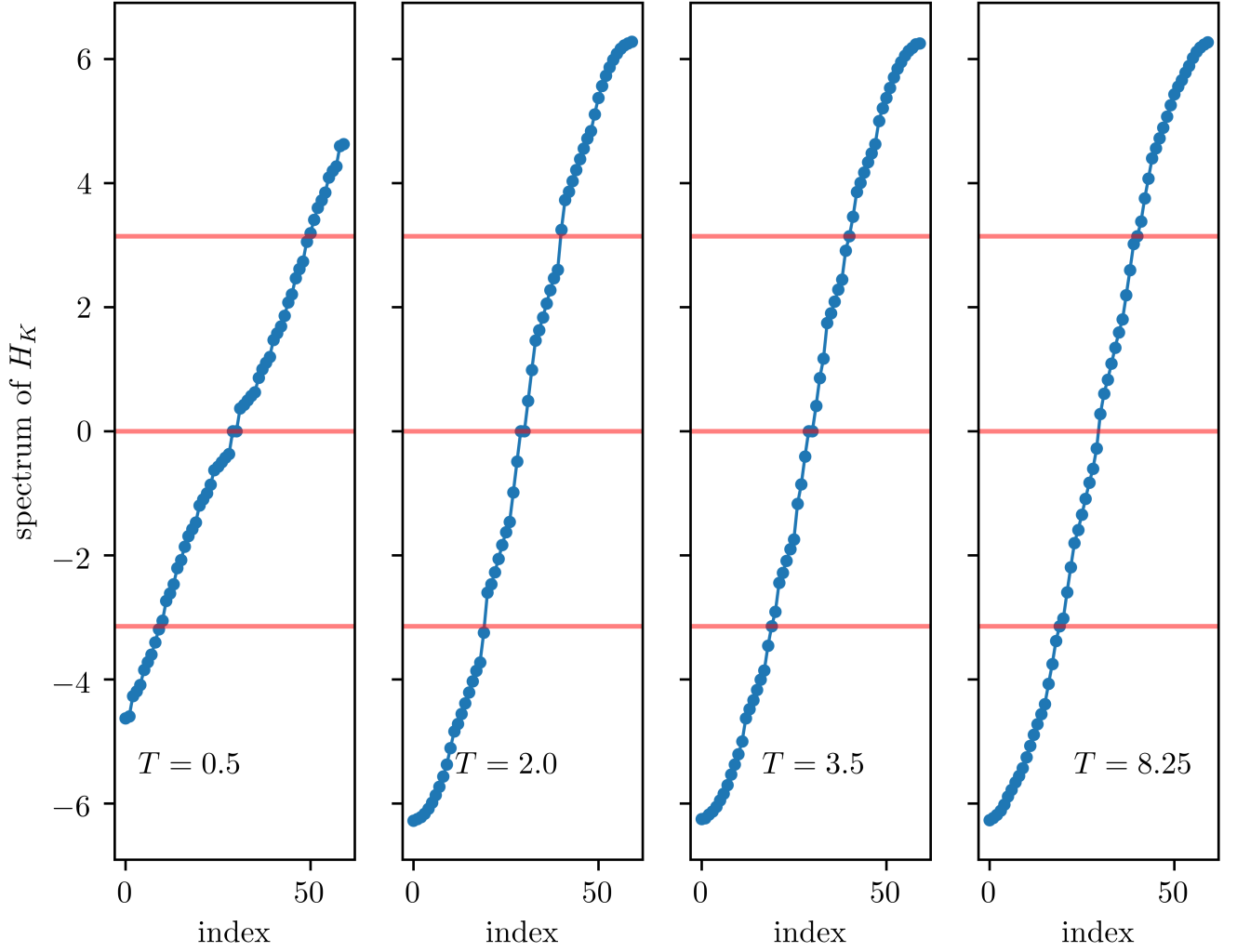


FIG. 6. The spectrum of H_K determined from performing Lanczos on the Floquet Hamiltonian with $J_z = 0.01$, $g = 0.3$ and $L = 10$. The corresponding b_n s are the green data in Fig. 5. The spectra correspond to ASZM ($T = 0.5$), ASZM ($T = 2.0$), ASZM-ASPM ($T = 3.5$) and, ASPM ($T = 5.5$). The horizontal red lines indicate the energies $0, \pm\pi$.

it. In particular,

$$A_\infty(nT) = \text{Tr} \left[W^n |1\rangle \langle 1| \right] \approx \text{Tr} \left[W^n \left(|\psi_0\rangle \langle \psi_0| + |\psi_\pi\rangle \langle \psi_\pi| \right) |1\rangle \langle 1| \right] \quad (85)$$

$$= \sum_{\lambda=0,\pi} \psi_{\lambda,1} \langle 1 | W^n | \psi_\lambda \rangle, \quad \psi_{\lambda,1} = \langle \psi_\lambda | 1 \rangle. \quad (86)$$

Above $|1\rangle$ is a state which is completely localized on the first site of the Krylov subspace. The approximation made in the second line involves replacing the complete set of states of W by only its edge modes $|\psi_{\lambda=0,\pi}\rangle$. Thus we are dropping all the bulk modes of W . Also note that, $\psi_{\lambda,1}$ is the normalized amplitude of the edge mode on the first site.

The results for A_∞ in Fig. 8 are compared to two different approximations. One is the data labeled as $d_{1,\lambda=0,\pi}$

where

$$d_{1,\lambda}(nT) = |\psi_{\lambda,1}|^2 e^{-\gamma_\lambda n} = |\psi_{\lambda,1}|^2 |\langle \psi_\lambda | W | \psi_\lambda \rangle|^n, \quad \lambda = 0, \pi. \quad (87)$$

The above expression uses the definition of the decay-rate in Eq. (65) accounting for the amplitude $\psi_{\lambda,1}$ of finding the particle on the first site, before the time-evolution. Since $|\psi_{0,\pi}\rangle$ edge modes are only approximate edge modes, Eq. (87) does lead to a decay. The data set labeled by $d_{2,\lambda=0,\pi}$ corresponds to approximating $\gamma_{0,\pi}$ by Eq. (78), thus

$$d_{2,\lambda}(nT) = |\psi_{\lambda,1}|^2 e^{-|\psi_{\lambda,N}|^2 n}, \quad \lambda = 0, \pi, \quad (88)$$

where $\psi_{\lambda,N}$ is the normalized amplitude of the $\lambda = 0, \pi$ approximate edge mode at the last site N .

We find that W , despite its truncation, agrees very well with ED. In addition, the two approximations to W given

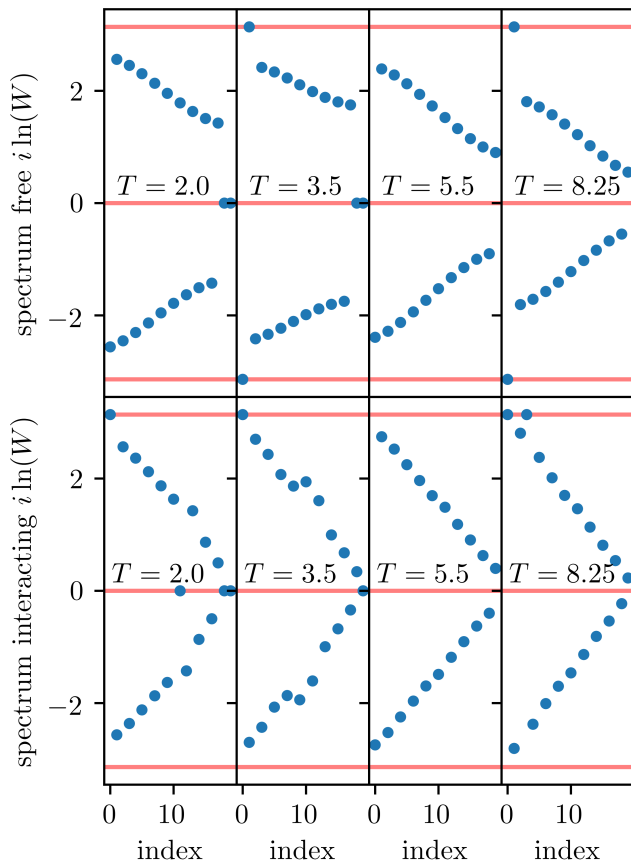


FIG. 7. Spectrum of $i \ln W$ for free example (upper row) and an interacting example with $J_z = 0.05$ (lower row). For all data $L = 10$ and W is a 20×20 matrix. In addition $g = 0.3$. The four different values of T are from left to right $T = 2.0, 3.5, 5.5, 8.25$. These correspond respectively to (A)SZM, (A)SZM-(A)SPM, trivial, and (A)SPM phases. The horizontal red lines indicate $0, \pm\pi$.

by Eq. (87) and Eq. (88) also agree well as far as capturing the decay rates are concerned. The approximations appear to not work quite so well for the second panel corresponding to the ASZM-ASPM phase ($T = 3.5$). This may be because when both almost strong modes are present, as they decay they influence each other through the bulk states in a way that our simple approximation has not accounted for. However, the agreement does improve with increasing system size (compare upper and lower panels for $T = 3.5$). In particular, when both ASZM and ASPM are present, the edge structure is more complex and has a 2×2 structure at each end (see Section V). This can make the effective system size of $L = 4$ (upper panels) look effectively shorter for an ASZM-ASPM phase as compared to an ASPM or an ASZM phase.

VIII. CONCLUSIONS

Almost strong edge modes are quasi-stable edge modes that have unusually long lifetimes so that they can co-exist with a metallic bulk for many drive cycles. These edge modes include both zero modes as well as π modes, where the latter show period doubled dynamics. It is notoriously hard to develop analytic methods for interacting and driven systems in general, and determining lifetimes of quasi-stable modes in particular. However in this paper we showed a promising route which involves mapping the dynamics of the edge mode operator to single particle dynamics in Krylov subspaces. While the detailed modeling of the Krylov subspace, such as the precise values of the hopping parameters, still requires the same computational costs as ED, yet when the operator of interest has some universal features, the Krylov subspace can have some general properties. For example, the Krylov subspace of maximally chaotic systems have certain universal features much discussed in the literature [33–36].

In this paper we showed that when the operators are strong modes or almost strong modes, they appear as stable or quasi-stable edge modes of Krylov subspaces with topological properties. For the examples studied in this paper, the Krylov subspaces are given by generalized SSH models with long range and spatially inhomogeneous hopping. Exploiting these topological structures can lead to better understanding of the long lifetimes of the almost strong modes.

Most studies on Krylov subspace dynamics use the Lanczos method where the generator of dynamics is a static Hamiltonian [32–36]. In studying Floquet systems, as we do in this paper, one has to adapt the Krylov subspace because the generator of dynamics is a unitary operator rather than a Hermitian operator. This lead us to derive the Krylov subspace using an alternate approach, known as the the Arnoldi iteration [27]. Topological features of the resulting chain were highlighted. A compact expression (c.f. Eq. (88)) for the lifetime of the edge modes was derived and compared with ED. In particular, we showed that the decay rate is simply determined by the probability of finding the particle on the last site N of the W matrix that generates the time-evolution in this Krylov subspace. This observation opens up the possibility of developing analytic tools for calculating the decay rate, such as by employing the WKB approximation.

Our methods can be generalized to study other kinds of slow dynamics such as dynamics of scar states[44–47]. It is also promising to perform a topological classification of the Krylov subspaces of edge modes of strongly interacting topological insulators, both static and Floquet [48–50].

Acknowledgements: The authors thank Sasha Abanov for helpful discussions. This work was supported by the US Department of Energy, Office of Science, Basic Energy Sciences, under Award No. DE-SC0010821.

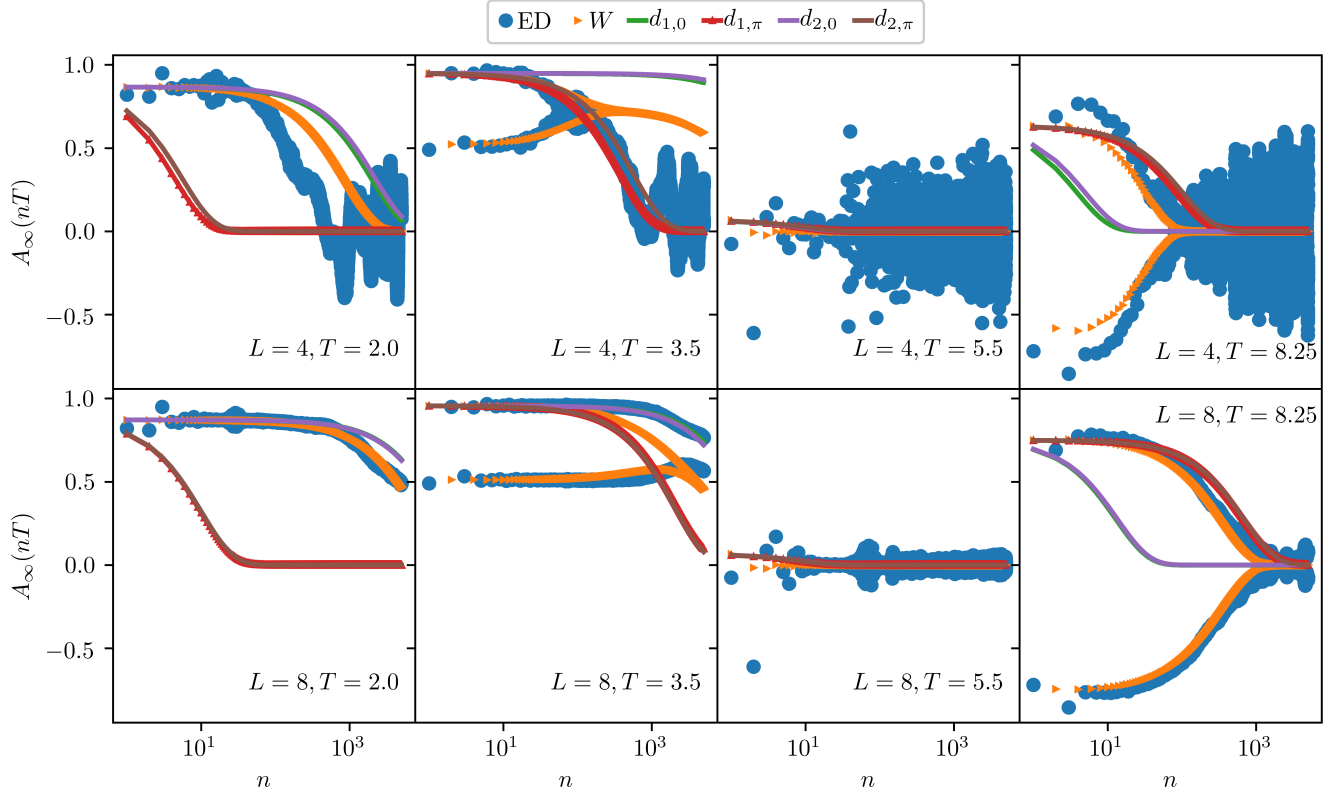


FIG. 8. Time evolution of approximate edge states of W (orange) for an interacting example ($J_z = 0.05$) and compared to A_∞ obtained from ED (blue). The top row is for a very small system size of $L = 4$ and the bottom row is for $L = 8$. The four columns compare four different phases. These are from left to right: ASZM phase ($T = 2.0$), ASZM-ASPM phase ($T = 3.5$), trivial phase ($T = 5.5$), and ASPM phase ($T = 8.25$). W is truncated to a 18×18 matrix, and the time-evolution generated by it (orange) is according to Eq. (86). The data labeled by $d_{1,\lambda}$, $d_{2,\lambda}$ with $\lambda = 0, \pi$ are two different approximations corresponding to Eq. (87) for $d_{1,\lambda}$ and Eq. (88) for $d_{2,\lambda}$.

-
- [1] A. Y. Kitaev, Unpaired majorana fermions in quantum wires, *Physics-Uspekhi* **44**, 131 (2001).
 - [2] S. Sachdev, *Quantum Phase Transitions*, Cambridge University Press (2011).
 - [3] B. A. Bernevig and (with T. L. Hughes), *Topological Insulator and Topological Superconductors*, Princeton University Press, Princeton (2013).
 - [4] A. Kitaev, Anyons in an exactly solved model and beyond, *Annals of Physics* **321**, 2 (2006), january Special Issue.
 - [5] C. Nayak, S. H. Simon, A. Stern, M. Freedman, and S. Das Sarma, Non-abelian anyons and topological quantum computation, *Rev. Mod. Phys.* **80**, 1083 (2008).
 - [6] J. Alicea, New directions in the pursuit of majorana fermions in solid state systems, *Reports on Progress in Physics* **75**, 076501 (2012).
 - [7] S. D. Sarma, M. Freedman, and C. Nayak, Majorana zero modes and topological quantum computation, *njp Quantum Information* **1**, 15001 (2015).
 - [8] K. Sacha and J. Zakrzewski, Time crystals: a review, *Reports on Progress in Physics* **81**, 016401 (2017).
 - [9] D. V. Else, C. Monroe, C. Nayak, and N. Y. Yao, Discrete time crystals, *Annual Review of Condensed Matter Physics* **11**, 467 (2020).
 - [10] V. Khemani, R. Moessner, and S. Sondhi, A brief history of time crystals, *arXiv:1910.10745* (2019).
 - [11] P. Fendley, Strong zero modes and eigenstate phase transitions in the xyz/interacting majorana chain, *Journal of Physics A: Mathematical and Theoretical* **49**, 30LT01 (2016).
 - [12] D. V. Else, P. Fendley, J. Kemp, and C. Nayak, Prethermal strong zero modes and topological qubits, *Phys. Rev. X* **7**, 041062 (2017).
 - [13] J. Kemp, N. Y. Yao, C. R. Laumann, and P. Fendley, Long coherence times for edge spins, *Journal of Statistical Mechanics: Theory and Experiment* **2017**, 063105 (2017).
 - [14] D. E. Parker, R. Vasseur, and T. Scaffidi, Topologically protected long edge coherence times in symmetry-broken phases, *Phys. Rev. Lett.* **122**, 240605 (2019).
 - [15] J. Kemp, N. Y. Yao, and C. R. Laumann, Symmetry-enhanced boundary qubits at infinite temperature, *Phys. Rev. Lett.* **125**, 200506 (2020).
 - [16] D. J. Yates, A. G. Abanov, and A. Mitra, Lifetime of al-

- most strong edge-mode operators in one-dimensional, interacting, symmetry protected topological phases, *Phys. Rev. Lett.* **124**, 206803 (2020).
- [17] D. J. Yates, A. G. Abanov, and A. Mitra, Dynamics of almost strong edge modes in spin chains away from integrability, *Phys. Rev. B* **102**, 195419 (2020).
- [18] L. Jiang, T. Kitagawa, J. Alicea, A. R. Akhmerov, D. Pekker, G. Refael, J. I. Cirac, E. Demler, M. D. Lukin, and P. Zoller, Majorana fermions in equilibrium and in driven cold-atom quantum wires, *Phys. Rev. Lett.* **106**, 220402 (2011).
- [19] V. M. Bastidas, C. Emary, G. Schaller, and T. Brandes, Nonequilibrium quantum phase transitions in the ising model, *Phys. Rev. A* **86**, 063627 (2012).
- [20] M. Thakurathi, A. A. Patel, D. Sen, and A. Dutta, Floquet generation of majorana end modes and topological invariants, *Phys. Rev. B* **88**, 155133 (2013).
- [21] J. K. Asbóth, B. Tarasinski, and P. Delplace, Chiral symmetry and bulk-boundary correspondence in periodically driven one-dimensional systems, *Phys. Rev. B* **90**, 125143 (2014).
- [22] D. J. Yates, F. H. L. Essler, and A. Mitra, Almost strong $(0, \pi)$ edge modes in clean interacting one-dimensional floquet systems, *Phys. Rev. B* **99**, 205419 (2019).
- [23] V. Khemani, A. Lazarides, R. Moessner, and S. L. Sondhi, Phase structure of driven quantum systems, *Phys. Rev. Lett.* **116**, 250401 (2016).
- [24] C. W. von Keyserlingk, V. Khemani, and S. L. Sondhi, Absolute stability and spatiotemporal long-range order in floquet systems, *Phys. Rev. B* **94**, 085112 (2016).
- [25] C. W. von Keyserlingk and S. L. Sondhi, Phase structure of one-dimensional interacting floquet systems. i. abelian symmetry-protected topological phases, *Phys. Rev. B* **93**, 245145 (2016).
- [26] C. W. von Keyserlingk and S. L. Sondhi, Phase structure of one-dimensional interacting floquet systems. ii. symmetry-broken phases, *Phys. Rev. B* **93**, 245146 (2016).
- [27] W. E. Arnoldi, The principle of minimized iterations in the solution of the matrix eigenvalue problem, *Quart. Appl. Math.* **9**, 17 (1951).
- [28] C. W. von Keyserlingk and S. L. Sondhi, Phase structure of one-dimensional interacting floquet systems. i. abelian symmetry-protected topological phases, *Phys. Rev. B* **93**, 245145 (2016).
- [29] V. Gritsev and A. Polkovnikov, Integrable Floquet dynamics, *SciPost Phys.* **2**, 021 (2017).
- [30] W. P. Su, J. R. Schrieffer, and A. J. Heeger, Solitons in polyacetylene, *Phys. Rev. Lett.* **42**, 1698 (1979).
- [31] W. P. Su, J. R. Schrieffer, and A. J. Heeger, Soliton excitations in polyacetylene, *Phys. Rev. B* **22**, 2099 (1980).
- [32] V. Vishwanath and G. Müller, *The Recursion Method: Applications to Many-Body Dynamics*, Springer, New York (2008).
- [33] D. E. Parker, X. Cao, A. Avdoshkin, T. Scaffidi, and E. Altman, A universal operator growth hypothesis, *Phys. Rev. X* **9**, 041017 (2019).
- [34] A. Dymarsky and A. Gorsky, Quantum chaos as delocalization in krylov space, *Phys. Rev. B* **102**, 085137 (2020).
- [35] J. Barbón, E. Rabinovici, R. Shir, and R. Sinha, On the evolution of operator complexity beyond scrambling, *Journal of High Energy Physics* **2019**, 264 (2019).
- [36] A. Avdoshkin and A. Dymarsky, Euclidean operator growth and quantum chaos, *Phys. Rev. Research* **2**, 043234 (2020).
- [37] D. J. Yates, A. G. Abanov, and A. Mitra, Long-lived π edge modes of interacting and disorder-free floquet spin chains, *arXiv:2021.0000* (2021).
- [38] R. A. Horn and C. R. Johnson, *Matrix Analysis*, Cambridge University Press, 2nd Edition (2013).
- [39] D. A. Abanin, W. De Roeck, and F. Huveneers, Exponentially slow heating in periodically driven many-body systems, *Phys. Rev. Lett.* **115**, 256803 (2015).
- [40] T. Kuwahara, T. Mori, and K. Saito, Floquet–magnus theory and generic transient dynamics in periodically driven many-body quantum systems, *Annals of Physics* **367**, 96 (2016).
- [41] T. Mori, T. Kuwahara, and K. Saito, Rigorous bound on energy absorption and generic relaxation in periodically driven quantum systems, *Phys. Rev. Lett.* **116**, 120401 (2016).
- [42] D. A. Abanin, W. De Roeck, W. W. Ho, and F. Huveneers, Effective hamiltonians, prethermalization, and slow energy absorption in periodically driven many-body systems, *Phys. Rev. B* **95**, 014112 (2017).
- [43] D. Abanin, W. De Roeck, W. W. Ho, and F. Huveneers, A rigorous theory of many-body prethermalization for periodically driven and closed quantum systems, *Communications in Mathematical Physics* **354**, 809 (2017).
- [44] S. Moudgalya, E. O’Brien, B. A. Bernevig, P. Fendley, and N. Regnault, Large classes of quantum scarred hamiltonians from matrix product states, *Phys. Rev. B* **102**, 085120 (2020).
- [45] C. J. Turner, A. A. Michailidis, D. A. Abanin, M. Serbyn, and Z. Papić, Weak ergodicity breaking from quantum many-body scars, *Nature Physics* **14**, 745 (2018).
- [46] W. W. Ho, S. Choi, H. Pichler, and M. D. Lukin, Periodic orbits, entanglement, and quantum many-body scars in constrained models: Matrix product state approach, *Phys. Rev. Lett.* **122**, 040603 (2019).
- [47] C.-J. Lin and O. I. Motrunich, Exact quantum many-body scar states in the rydberg-blockaded atom chain, *Phys. Rev. Lett.* **122**, 173401 (2019).
- [48] L. Fidkowski and A. Kitaev, Effects of interactions on the topological classification of free fermion systems, *Phys. Rev. B* **81**, 134509 (2010).
- [49] A. C. Potter, T. Morimoto, and A. Vishwanath, Classification of interacting topological floquet phases in one dimension, *Phys. Rev. X* **6**, 041001 (2016).
- [50] D. V. Else and C. Nayak, Classification of topological phases in periodically driven interacting systems, *Phys. Rev. B* **93**, 201103 (2016).